Neuromethods 130

Springer Protocols

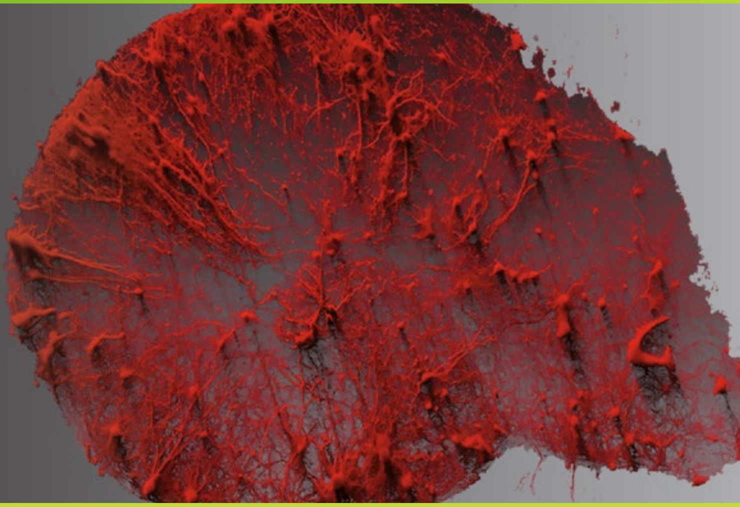

Sandrine Parrot
Luc Denoroy *Editors*

Biochemical Approaches for Glutamatergic Neurotransmission

Humana Press

Chapter 5

Imaging Glutamate with Genetically Encoded Fluorescent Sensors

Gerard J. Broussard, Elizabeth K. Unger, Ruqiang Liang, Brian P. McGrew, and Lin Tian

Abstract

Superimposed on the vast and complex synaptic network is a largely invisible set of chemical inputs, such as neurotransmitters and neuromodulators, that exert a profound influence on brain function across many structures and temporal scales. Thus, the determination of the spatiotemporal relationships between these chemical signals with synaptic resolution in the intact brain is essential to decipher the codes for transferring information across circuitry and systems. Recent advances in imaging technology have been employed to determine the extent of spatial and temporal neurotransmitter dynamics in the brain, especially glutamate, the most abundant excitatory neurotransmitter. Here, we discuss recent imaging approaches, particularly with a focus on the design and application of genetically encoded indicator iGluSnFR, in analyzing glutamate transients in vitro, ex vivo, and in vivo.

Key words Glutamate, iGluSnFR, Fluorescent sensor, Genetically encoded indicators of neural activity, Protein engineering, Fluorescent functional imaging

1 Introduction

1.1 Glutamate Signaling in the Central Nervous System

Glutamate (Glu) is an amino acid used in a variety of contexts across all known kingdoms of life. In central nervous systems (CNS), Glu acts as the primary excitatory neurotransmitter [1]. As such, glutamatergic signaling forms the basis for information transfer in the brain. In addition to its role as key mediator of synaptic information relay, Glu signaling can induce de novo growth of functional synapses [2] and is also crucial in modifying synaptic strength during phenomena such as long-term potentiation and long-term depression [3]. Glutamate also serves as an essential component of the complex signaling interactions between neurons and astrocytes, the most prominent glial cell type in the CNS [4].

Gerard J. Broussard and Elizabeth K. Unger contributed equally to this work.

Sandrine Parrot and Luc Denoroy (eds.), *Biochemical Approaches for Glutamatergic Neurotransmission*, Neuromethods, vol. 130, DOI 10.1007/978-1-4939-7228-9_5, © Springer Science+Business Media LLC 2018

Finally, dysregulation of Glu has been implicated in the pathogenesis of acute neurological insults, such as traumatic brain injury and stroke [5], and degenerative neurological disorders, including multiple sclerosis, Alzheimer disease, Huntington disease, Parkinson disease, amyotrophic lateral sclerosis, and others [6].

Glutamate signaling has a correspondingly wide range of spatial and temporal dynamics. Following action potential-evoked vesicular release, synaptic Glu concentrations rapidly increase to the low millimolar range [7]. Typically, clearance of synaptic Glu occurs with a time constant of decay of around 1 ms and is handled by a combination of diffusion and active reuptake by a family of excitatory amino acid transporters, which are primarily localized to nearby astrocytes [7, 8]. While the distance between synapses in many brain regions is typically less than 1 μm [9], spillover of Glu during synaptic release can potentially affect neighboring cells over 10 μm away [10]. Meanwhile, Glu tone within the extra-synaptic space is primarily regulated by astrocytes and sits at a concentration within the high nanomolar to low micromolar range, dependent on local patterning of Glu release and reuptake sites [11].

Glutamate receptors are broken into two primary subtypes based on whether they are mediated by metabotropic or ionotropic Glu receptors (mGluRs or iGluRs, respectively). The human mGluR family is made up of eight G-protein-coupled receptors, subdivided into three groups based on mechanism and pharmacology. Group I mGluRs exert their action by activating phospholipase C, while mGluRs in groups II and III inhibit production of cyclic AMP [12]. Alternatively, the rapid excitatory signaling at synapses is mediated by iGluRs, which are ligand-gated cation channels classically categorized into three pharmacologically identified subtypes: *N*-methyl-D-aspartate (NMDA) receptors, α-amino-3-hydroxy-5-methyl-4-isoaxazole propionate (AMPA) receptors, and kainate receptors [13].

Physiological consequences of activation of Glu receptors are dictated by receptor affinity, kinetics, and localization. Affinities of these various receptor types range over about three orders of magnitude, with the highest affinities (~1–10 μmol/L) found among the NMDA receptors and most mGluRs, while the lowest affinity receptors are non-NMDA ionotropic receptors and mGluR7, with affinities of 500 μmol/L and 1000 μmol/L, respectively [14, 15]. Activation kinetics of Glu receptors range from ones of milliseconds for non-NMDA receptors to tens of milliseconds for all other receptor subtypes [14, 16, 17]. In the CNS, ionotropic Glu receptors localize primarily to synaptic and perisynaptic sites, while mGluRs can be found in a range of different neuronal cellular compartments [18], as well as studding the surface of glial cells, such as astrocytes [19].

Given the importance of glutamatergic signaling in the brain, there is a pressing need for technology to enable direct and precise measurements of Glu signaling at the synaptic and microcircuit levels across various temporal scales in behaving animals.

1.2 Current Approaches for Direct Measurement of Glutamate in the Brain

Analytic chemistry has provided useful insights about the concentrations of Glu in the brain via microdialysis [20], glutamate oxidase-enabled cyclic voltammetry [21], and semisynthetic sensors [22–24]. However, microdialysis measurement surface areas are typically in the range of 1000 μm^2, while concentration measurements can be taken on intervals ranging from ones to tens of minutes [20]. Whereas cyclic voltammetry does allow for rapid temporal precision, typical probe size is in the range of 30–250 μm^2 [25, 26]. This approach also lacks cellular resolution, can potentially lose sensitivity in biological tissues, and can be confounded by other potential sources of naturally occurring electroactive molecules [27]. Both methods thus fall far short of the spatial resolution required to track Glu changes in the subcellular domains in vivo.

Alternatively, microscopy-based measurements can provide the temporal and spatial resolution required to image Glu transients in intact tissue. Advances in the speed, depth penetration, and spatial resolution of fluorescence microscopy techniques have extended our ability to measure glutamatergic signaling noninvasively. Optical recordings from hundreds to thousands of neuronal elements across large tissue areas and volumes are now possible with single-cell or single-synapse resolution, both in vitro and in vivo. One-photon imaging with ultrafast cameras permits very rapid (>1 kHz) subcellular-resolution optical recordings from millimeter-scale surface regions. In contrast, multiphoton microscopy allows noninvasive functional imaging from up to ~1 mm tissue depths across near-millimeter fields of view, with subsecond temporal and submicron spatial resolution. In addition, both one- and multiphoton imaging can be performed in behaving animals and through endoscopes or fiber optics, allowing measurements from deep brain structures, such as the striatum or brainstem. As imaging technologies become more developed and available for routine laboratory applications, high-quality optical probes have also been developed in parallel (for details, see Sect. 1.5).

1.3 Imaging Probes for Glutamate

To directly measure Glu with molecular specificity, an array of Glu probes including small molecule-protein hybrids and genetically encoded sensors, have been developed to be compatible with fluorescent microscopy. For example, Glu optical sensor (EOS) is a hybrid sensor constructed from the S1S2 Glu-binding domain of the AMPA receptor GluR2 subunit and a small-molecule dye [22]. One of the EOS variants exhibited an increase of 48% in $\Delta F/F_{\max}$ (maximal fluorescence changes over basal fluorescence) upon Glu binding (K_d = 1.57 μmol/L) when measured at the surface of HeLa cells and about a 1–2% fluorescence increase in mouse somatosensory cortical neurons following limb movement. However, the use of such sensors generally requires application of an exogenous cofactor, such as a small molecule dye [22], limiting their utility for in vivo deployment and barring their use in experiments requiring chronic measurements.

More recently, Snifit (SNAP-tag-based indicator proteins with a fluorescent intramolecular tether)-based sensors for optical measurement of Glu have been developed. A Glu-Snifit is a fusion protein with three components, an ionotropic Glu receptor 5 (iGluR5), a CLIP-tag with a synthetic donor fluorophore, and a SNAP-tag bearing another synthetic acceptor fluorophore conjugated with O6-benzylguanine (BG)-polyethylene glycol (PEG) 11-Cy5-glutamate as an antagonist [23]. In the absence of Glu, the Snifit adopts a closed conformation and Förster resonance energy transfer (FRET) efficiency increases. In the presence of Glu, the intramolecular antagonist is displaced to shift Snifit toward an open state with a resultant decrease in FRET efficiency. The Snifit-iGluR5 showed a ΔR_{max} (maximal fluorescence change in donor-acceptor ratio) of 1.93 and an apparent K_d of 12 μmol/L for Glu in HEK 293T cells. Further optimization and characterization are likely needed to allow in situ detection of physiological levels of Glu release and uptake by living neurons and intact circuitry.

1.4 Genetically Encoded Fluorescent Indicators for Neural Activity

Genetically encoded indicators of neural activity (GINAs) are a set of tools that permit noninvasive, direct, specific, and long-term measurements of changes in calcium, voltage, Glu, and vesicular release over various temporal scales within genetically specified cells or synapses, and within or across neural circuits of live animals (reviewed in [28, 29]).

GINAs are proteins comprising a sensor and a fluorescent-reporter domain that can act as optical readouts of signals propagated within the nervous system. Conformational changes, upon binding of an analyte by the sensor domain, drive a fractional modulation of the reporter-domain fluorescence output (often referred to as $\Delta F/F$). Applications of these sensors have facilitated large-scale recording of neural activity in genetically identified neurons or glial cells. In addition, genetically encoded sensors without overlapped spectra have been engineered to allow multiplex imaging or to combine with optogenetic actuators, which has opened many possibilities for sophisticated analysis of neural activity. Genetically encoded sensors can be selectively targeted to genetically defined cell types or subcellular locations, such as axons or dendritic spines, or to cells with specific anatomical connectivity. Finally, these sensors can be stably expressed over a long time (from days to several months), allowing the study of how neural-activity patterns change with learning, development, or disease progression.

The first GINAs to gain widespread use for in vivo detection of neural activity were genetically encoded calcium indicators (GECIs) designed to detect action potential-related calcium fluxes. This subset of GINAs includes single-fluorescent protein (FP)-based GCaMP family and FRET-based Cameleon family [30–34]. For example, in the scaffold of GCaMPs, calmodulin (CaM) binds the RS20 peptide from smooth muscle myosin light chain kinase in the presence of calcium; this coupling reverses when calcium is absent. The sensor domain transduces conformational changes of calcium binding to a change in the fluorescence intensity through its coupling with the circularly permutated green fluorescent protein (GFP) (cpGFP; see [35]). The crystal structure of GCaMP2 has revealed that the rearrangement of the CaM/RS20 domain upon calcium binding brings an arginine at position 377 into proximity to coordinate the chromophore of cpGFP into a deprotonated bright state [36]. Iterative improvements have since been made to this original design through rational design combined with directed evolution, which has produced a series of widely applicable sensors, GCaMP3/5/6, for calcium imaging in awake, behaving animals [34, 37–41]. Studies have also been conducted examining changes to calcium dynamics with temporal scales ranging from single milliseconds [42, 43] to learning-associated [44] and plasticity [45] changes unfolding over months. While optimization of calcium indication continues with the focus on faster kinetics, superior brightness, and sensitivity for detecting subthreshold activity, the genetically encoded voltage sensors have also been intensively optimized to facilitate voltage imaging both at mesoscopic and cellular resolutions in living behaving mammals [46].

1.5 Design of Genetically Encoded Fluorescent Indicators for Glutamate

Despite many advantages presented by GECIs as a tool for neuroscience, in certain contexts, a GINA designed to directly detect Glu is superior or complementary. For example, coupling between calcium influx and Glu release from presynaptic compartments can be highly nonlinear, such as during the process of synaptic facilitation or depression [47]. A Glu sensor expressed in postsynaptic cells could therefore more accurately reflect the influence of presynaptic activation on receiving-cell physiology. Additionally, in experiments involving bulk imaging of neural tissue, GECIs report primarily spiking activity in cells within the imaged volume. Whereas a Glu sensor grants experimental access to subthreshold synaptic activation [48]. Finally, not all Glu-initiated neural signaling events involve obligate calcium influx (see [49]). The ability to perform multiplex measurement of Glu signaling combined with measurement of calcium, voltage, and circuitry manipulation tools is even more important.

To date, protein-engineering efforts have led to the development of a series of single-FP or FRET-based Glu sensors consisting of the bacterial glutamate/aspartate-binding protein, GltI (also called YbeJ). GltI is the periplasmic component of the ATP-binding–cassette transporter complex for aspartate and Glu in *Escherichia coli* (*E. coli*; [50]). GltI is a member of the periplasmic binding protein (PBP) superfamily, which is typically composed of two domains that undergo a Venus flytrap-like hinge-twist motion upon ligand binding [51]. This conformational change serves as the basis for Glu sensitivity in FRET-based Glu sensors, including fluorescent indicator protein for Glu FLIPE [52] and SuperGluSnFR [53], or the single-FP-based iGluSnFR [54].

To date, iGluSnFR is the only Glu indicator that has been widely used for in vivo imaging. The single-FP-based iGluSnFR was developed by inserting cpGFP, the same cpGFP developed for GCaMP2 [31], into Gltl. Upon Glu binding, conformational adjustments result in changes in the chromophore environment, thus transforming the ligand-binding event into fluorescent intensity changes. A critical challenge in the construction of iGluSnFR (and indeed, any sensor with similar design properties) is to determine the optimal insertion site in Gltl for cpGFP. One approach to rational design of the insertion position is analysis of change in the dihedral-bond angle of alpha carbons (i.e., bond angle formed by four sequential amino acids) upon ligand binding (for details, please see Sect. 2). To maximize the $\Delta F/F$ and kinetics in response to Glu, linker regions between Gltl and cpGFP were optimized via site-saturated mutagenesis. Because of the close proximity of the linkers to the chromophore, those linkers are well situated to modify chromophore-solvent access and the stability of apo- and bound conformations [30, 33, 55]. A sizable portion of the possible 160,000 variants was screened from each cpGFP insertion site.

The final design of iGluSnFR produced a sensor with greater $\Delta F/F$ (~4.5) and affinity (K_d ~ 4 μmol/L) to Glu than previously available genetically encoded Glu sensors. Additionally, the "on rate" for binding was too fast to be determined by stopped-flow cytometry (~6 ms resolution), suggesting that the kinetics of iGluSnFR may be sufficiently rapid to faithfully track even the fast component of Glu transients at the synaptic cleft [7].

The superior intrinsic properties of iGluSnFR permit in vivo applications. iGluSnFR has proven to be useful in tracking phenomena at spatial scales ranging from subcellular to mesoscopic imaging of entire brain regions [48–64]. As with all genetic tools, iGluSnFR can be targeted to genetically defined cell populations, and has thus also proven ideal for unraveling the contributions to dynamics of the local brain circuitry made by specific neural

[56, 57] and even glial cells [65–69]. Finally, the superior kinetics of iGluSnFR, coupled with the rapidity of Glu transients themselves, have allowed wide-field imaging with greater temporal precision than is possible with current calcium indicators [48].

1.6 Systematization of Sensor Characterization and Validation In Vitro, Ex Vivo, and In Vivo

While GINAs have made massive strides in the past decade, further development is an ongoing task. The ultimate goal of GINA development is to obtain an appropriate signal-to-noise ratio (SNR) that matches the system studied for in vivo preparations. Because of imaging depth and motion artifacts, in vivo imaging has very demanding signal-to-noise requirements. To maximize the SNR and to achieve the best imaging outcomes, the intrinsic properties of sensors, including photophysical properties, specificity, kinetics, and affinity, must be matched to the physiological properties of measured signaling events, including the amplitude and transient size, time course, and frequency, as well as to the imaging system properties, such as speed, resolution, sensitivity, and depth penetration. In addition, it is essential to optimize the expression level for minimizing long-term cellular expression effects, such as clumping and off-target fluorescence species and interference with endogenous signaling pathways. End users must choose the most appropriate sensors and imaging systems; therefore, calibrating and comparing each sensor's performance under the same experimental conditions is critical.

Recently, a highly optimized pipeline for novel sensor development has been established in our lab and others, from concept to protein purification and validation in cultured cells, brain slices, and in vivo (Fig. 1) [28, 70, 71]. For probe development, in silico-aided design along with high-throughput genetic cloning strategies are becoming a standard set of tools for the modern protein engineer. To balance between throughput and in vivo predictability, with the goal of finally demonstrating the capability of these sensors in living animals, we carry out a systematic characterization

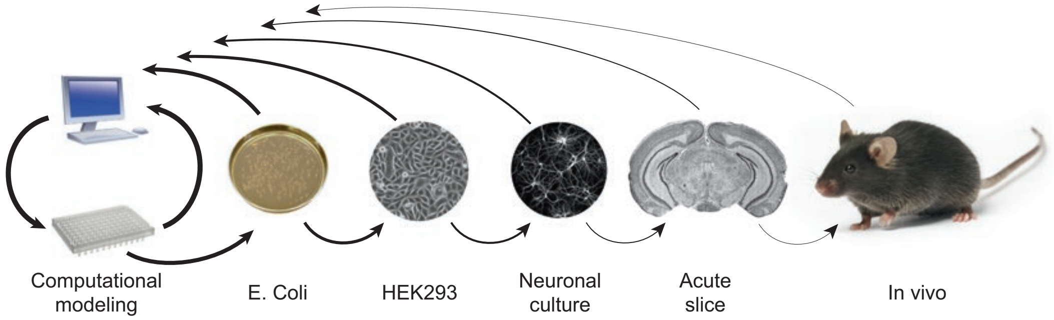

Fig. 1 Iterative workflow for testing variants in increasingly complex biological systems from computational design, *E. coli*, HEK293 cells, dissociated neuronal culture, acute brain slice, and in vivo

in *E. coli*-derived protein, in mammalian cells, in dissociated neuronal culture, and in acute brain slices and in vivo. This multiple-layer characterization also provides feedback for improving overall design and generation of libraries to iteratively optimize the intrinsic properties of the sensors. It is critical that the entire design process is best thought of as a closed loop where each step in the process informs earlier steps. Through iterative design and experimental validation, we expect to obtain lead sensors with the required design specifications and SNR for in vivo imaging. Here, we discuss each of these steps for developing Glu sensors, which can be broadly utilized for other sensor development.

2 Materials and Methods

2.1 Modeling Optimal Insertion Site of cpGFP with Rosetta

Single-wavelength, genetically encoded, fluorescent sensors undergo specific conformational changes induced by ligand-protein binding, resulting in a fluorescence readout. Molecular modeling is an indispensable tool to guide the engineering of this process. For this purpose, we use Rosetta, a suite of software libraries for macromolecular modeling [72].

For ligands having a natural bacterial PBP, a cpGFP insertion site can be predicted by maximizing the difference of C-alpha torsion between the backbones of the apo- and ligand-bound PBP scaffolds with the UCSF Chimera program [73]. The resultant structure of the cpGFP insertion can be simulated with rosetta_cm.xml script using the structures of the PBP (for example, Gltl PDB ID: 2VHA) and cpGFP (PDB ID: 3EVP) as templates [74]. As the Glu-unbound state of Gltl is not available, homologous analysis with maltose-binding protein (MBP) was used to predict the insertion site of cpGFP in Gltl (Fig. 2). Similar to GltI, MBP is a PBP family member, and the two proteins share a high degree of homology.

The psi/phi torsion changes between apo- and ligand-bound conformations of PBP scaffold protein can be calculated by extracting these torsions using Chimera. These values can be accessed from the Render by Attribute submenu in the Structure Analysis submenu under the Tools menu. After exporting these values into a text file, the difference can be calculated with Excel. Importantly, attention to correct residue numbering is needed because the two sequences between apo- and ligand-bound conformations may not necessarily be the same. cpGFP should be inserted at sites that show a large alpha torsion. For example, in the case of iMaltSnFR an amino acid position was identified near the hinge of the MBP that undergoes large torsional changes upon binding of maltose [55]. Through homologous analysis, it was predicted that position 249 in Gltl would be a potential insertion site for cpGFP (Fig. 2c).

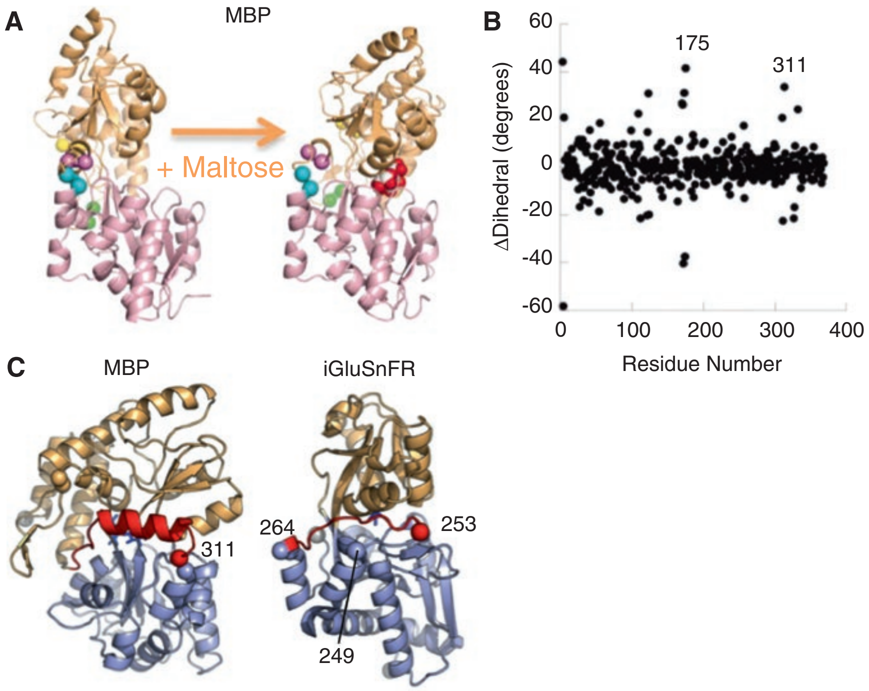

Fig. 2 (**a**) Crystal structure of iMaltSnFR with and without maltose bound, and (**b**) C-α-torsion at each residue (reproduced with permission from Marvin et al. (2011) [55]). (**c**) Comparison between iMaltSnFR and iGluSnFR (reproduced with permission from Marvin et al. (2013) [54])

Based on this initial site combined with optimization, insertion of cpGFP into position 253 of GltI yielded the basis for the final iGluSnFR design.

2.2 Directed Evolution

Computer modeling is an excellent way to begin the process of redesigning a protein; however, not all physical properties of the protein are, or even can be, explored. Even with sophisticated computer modeling algorithms such as the ones available in Rosetta, fully predicting the most-beneficial mutations for a specific protein function is still difficult. The idea of directed evolution is to introduce mutations in an iterative manner, while applying selection pressure to gradually enhance specific properties of the protein, be it thermal stability, brightness, binding affinity, and so forth. Mutations may be completely random, as in error-prone polymerase chain reaction (PCR), or they may be targeted to certain positions deemed most likely to yield the most promising results, as in site-saturated mutagenesis. Selection pressure is then applied by subjecting the variants to a test and promoting only the best performers to the next round of mutagenesis (Fig. 3).

2.2.1 Site-Directed Mutagenesis

Full sampling of all possible amino acids at all positions within a protein is generally an infeasible approach. For example, iGluSnFR consists of 562 amino acids. If we were to sample all 20 residues at all 562 positions, the number of possible combinations would be incomprehensibly large and well beyond the capacity of any lab to test, not to mention that most of those combinations would produce improperly folded or nonfunctional proteins. The number of possible variants can be reduced by focusing only on sites expected to influence ligand-binding-induced fluorescence change. The strength of this approach is exemplified by the linker screen used in the creation of iGluSnFR. By focusing on only the four amino acids connecting GltI to cpGFP, libraries of only 1.6×10^5 candidates were created.

Traditionally, site-saturated mutagenesis is performed by creating primers with degenerate codons at the position to be mutated. For example, the primer will include 10–15 matching bases, then the degenerative codon NNK or NNS, followed by another 10–15 matching bases. The purpose of including a K (G or T) or S (G or C) in the third position is to reduce the possibility of producing a stop codon (TAA or TGA). Eliminating the third stop codon (TAG) is not possible because both methionine and tryptophan only have one codon: ATG and TGG, respectively; thus, G must be a possibility in the third position to cover all 20 amino acids. The advantage of such a strategy is that a single oligo can be created that contains codons for all 20 amino acids. One major criticism of this strategy is that there is not equal probability of randomly selecting each amino acid, and some residues will be over-represented, while others will be under-represented. For instance, using either an NNK or NNS primer, there are 32 possible codons, with three possible codons for leucine, serine, and arginine; two possible codons for valine, glycine, alanine, threonine, and proline; and one possible codon for each of the rest. An alternative strategy is to generate one primer for each amino acid [75], which ensures equal probability of each one but is more costly and time-consuming. However, duplicate variants are expected within a screen, even one with equal probability distribution. Thus, to ensure all 20 amino acids are represented, many more samples are tested than the number of possibilities. For a typical library at one position with 20 possible amino acids, 96 colonies of variants are picked and tested. Even with an unequal probability distribution, this setup is usually sufficient to obtain at least one instance of each amino acid. The results of the screen should not depend on the number of times the amino acid is tested; the only consideration should be how many colonies need to be tested to ensure each amino acid is represented in the dataset.

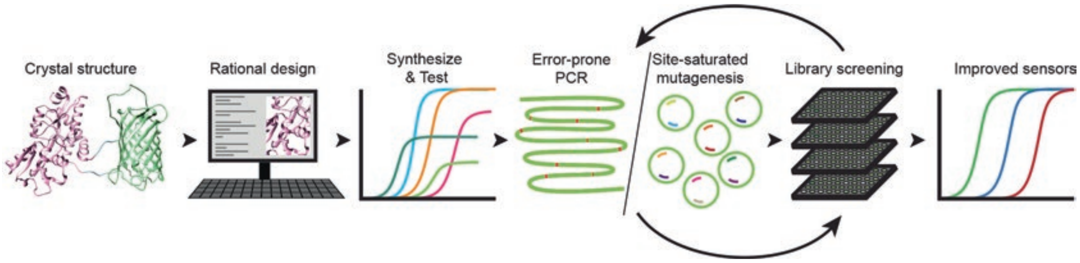

Fig. 3 Workflow for performing directed evolution

There are several methods for introducing mutations, insertions, or deletions into the template plasmid (Fig. 4). If only one or two positions are being interrogated, simple methods can be employed, such as QuikChange® mutagenesis. With QuikChange®, complementary primers containing the mutated codon are used in a PCR, which then linearly amplifies the plasmid while incorporating the mutation. The template is then digested away using DpnI, and the nicked plasmids are transformed to bacteria. The efficiency of QuikChange® is heavily impacted by the formation of primer dimers. One solution is to perform separate parallel reactions with a single primer each [76]. Another solution is to offset the primers such that they have a shorter region of homology with a melting temperature lower than that of the annealing temperature of the PCR [77]. A similar method is site-directed mutagenesis with blunt-end ligation, where primers are designed to amplify the entire plasmid, while introducing the mutation at the end of one or both of the primers. Because there is no homology between the primers, primer dimer is not an issue and the plasmid is linearized and exponentially amplified in a PCR. This method makes it easy to introduce insertions, because additional basepairs at the end of the primer do not affect the binding affinity. One concern is that longer primers occasionally will be missing the last basepair or two, and thus the sequence must be confirmed afterward. This method requires phosphorylated primers and a high-performance polymerase that does not leave an A-tail, such as Phusion (NEB) or Hotstart Taq (NEB). Alternatively, the added A overhang from a traditional Taq-based PCR may be digested away using Klenow (NEB). The template DNA is destroyed by DpnI digestion, and the ends of the linearized plasmid are ligated together and transformed to bacteria. While blunt-end ligation can be more efficient than QuikChange®, it requires the added steps and cost of phosphorylating the primers.

While QuikChange® and blunt-end ligation are traditionally used to introduce one mutation at time, for libraries at two distant positions, we typically use circular polymerase extension cloning (CPEC) [78]. Two sets of complementary primers are designed, each spanning one of the positions to be mutated. In the first PCR

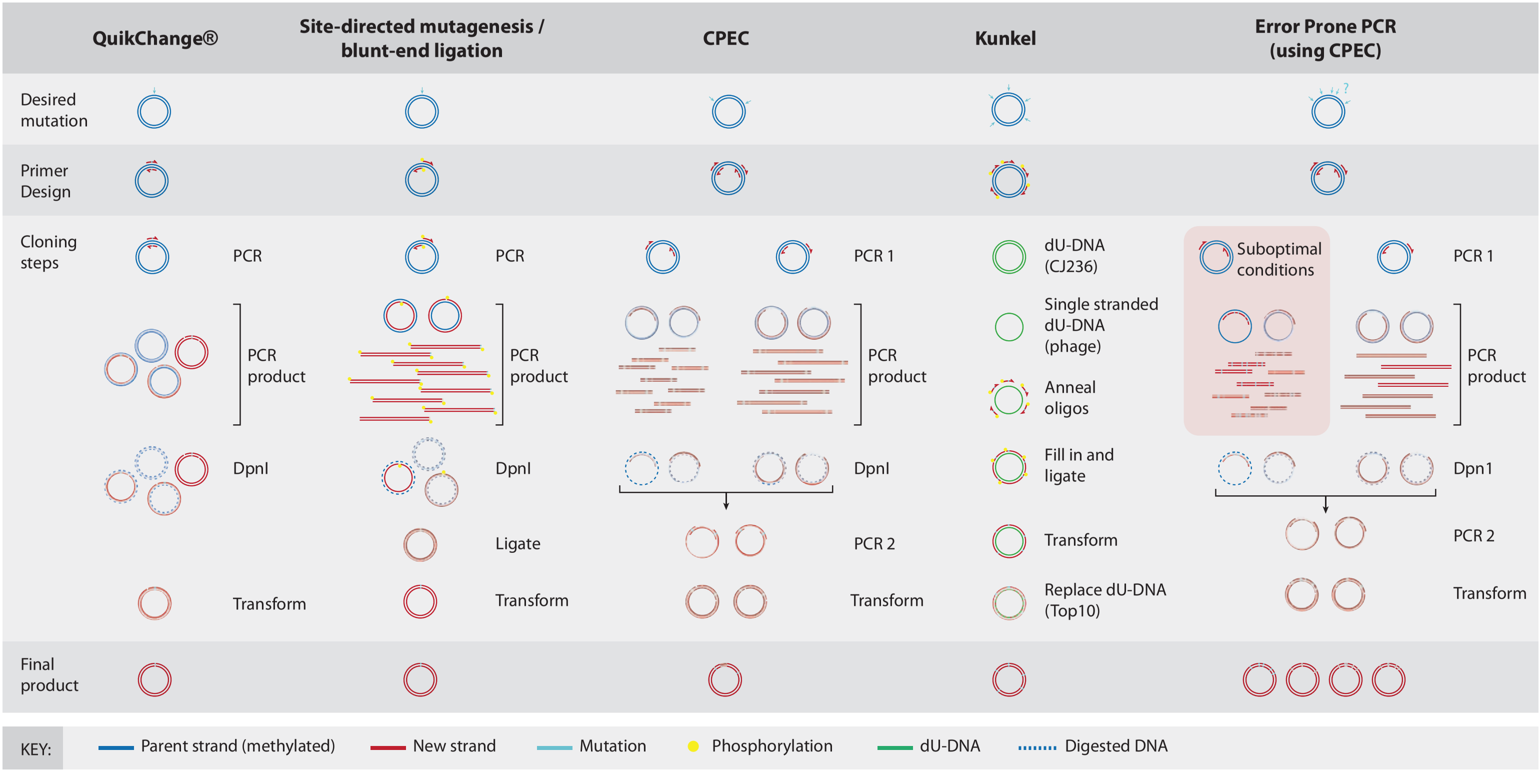
QuikChange®
Site-directed mutagenesis / blunt-end ligation
CPEC
Kunkel
Error Prone PCR (using CPEC)
Desired mutation
Primer Design
Cloning steps
PCR
PCR product
DpnI
Transform
PCR
PCR product
DpnI
Ligate
Transform
PCR 1
PCR product
DpnI
PCR 2
Transform
dU-DNA (CJ236)
Single stranded dU-DNA (phage)
Anneal oligos
Fill in and ligate
Transform
Replace dU-DNA (Top10)
Suboptimal conditions
PCR 1
PCR product
Dpn1
PCR 2
Transform
Final product
KEY:
Parent strand (methylated)
New strand
Mutation
Phosphorylation
dU-DNA
Digested DNA

Fig. 4 Comparison of different cloning methods used to introduce random or targeted mutations into a genetically encoded sensor

step, noncomplementary primers are added to two separate reactions, such that each reaction will exponentially amplify a section of the plasmid between the mutated positions. Template DNA is digested away, and then the products are combined in the second PCR step, wherein the two reactions are mixed. Because the initial primers were designed to be complementary, each amplified region can now serve as a primer for the remainder of the plasmid. There is no amplification at this step, so fewer cycles need to be run. Nicked plasmids are then transformed into bacteria. Both QuikChange® and CPEC are robust and easy to use, however, it must be noted that the probability of two matching primers coming together in the same plasmid is quite low. Thus, we rely on the mismatch repair machinery within the bacteria to correct these errors and to ligate the nicked plasmids.

While there are several methods for introducing mutations at more than two positions, one of the most efficient methods is Kunkel mutagenesis [79]. In this method, unidirectional primers are designed for each mutation (one primer per mutation). The plasmid is transformed into a strain of bacteria lacking a uracil-degrading enzyme, CJ236 (−UNG). The bacteria are then infected with a bacteriophage (M13K07), which creates single-stranded, uracil-containing DNA. Single-stranded dU-DNA is harvested, and phosphorylated oligos containing each mutation are annealed to the template. The gaps are then filled in and ligated together using a T7 polymerase and a T4 ligase. Note that oligos must be annealed on the same strand as the f1 origin for the process to work. The plasmid is then transformed to a normal bacterial strain capable of degrading uracil (+UNG), for example Top10 (Thermo Fisher), DH5α (NEB), or HB101 (Thermo Fisher), which will degrade the uracil-containing parent strand and replace it using the mutated strand to create a double-stranded, mutated plasmid. We have successfully introduced as many as 18 separate mutations in a single round of Kunkel mutagenesis with a surprisingly high success rate. Generating the single-stranded dU-DNA can be time-consuming, but is much faster than repeated rounds of QuikChange®. Including an additional oligo that destroys a restriction site and then digesting with that restriction enzyme allows selection of only those plasmids that have incorporated the new primers [80]. In many cases, most or all of the primers will bind in a single plasmid.

An alternative method of Kunkel mutagenesis skips the generation of single-stranded dU-DNA. In this method, phosphorylated oligos are annealed directly to the parent plasmid. Then the gaps are filled in by a polymerase and ligated together as above. The parent plasmid is digested away using DpnI, and a single primer is added to the remaining strand in a single-step PCR to produce the complementary strand. The nicked plasmid is then transformed to bacteria.

2.2.2 Error-Prone PCR

Rather than introducing mutations at specific locations, introducing mutations at random is often advantageous, especially when computational models for rational design are not possible. One method for doing so is error-prone PCR (EPP), where the PCR conditions are altered to be suboptimal, which produces higher error rates [81]. Any combination of adding excess $MgCl_2$ or $MnCl_2$, adding unequal concentrations of each nucleotide, and using a low-fidelity polymerase can achieve this result. Often, these mutations will be single-point mutations but may also be deletions or insertions, which may lead to frameshifts. To introduce mutations only to the gene being interrogated rather than the entire plasmid, the gene may be amplified by EPP and then inserted as a library into the vector via ligation cloning, CPEC (step 2), or Gateway® cloning [82]. Although the efficiency of producing improvements in the engineered protein is lower than with site-directed mutagenesis, this method allows for the exploration of many more possibilities and the potential for unpredicted benefits.

2.3 High-Throughput Bacterial Screening

2.3.1 Determining In Vitro ΔF/F

In silico design methods result in a large number of potentially suitable target protein structures. However, their true utility must be tested in vitro. We performed our initial screening on a bacterial platform, which is fast and fairly easy. We began with a bacterial expression vector, pRSET-A (Thermo Fisher), which contains a conditional promoter, and a 6×-his tag for protein purification. Plasmid libraries are transformed to a bacterial strain lacking several protein degradation enzymes, BL21(DE3)(Thermo Fisher). This strain contains a T7 RNA polymerase, which can be induced by addition of Isopropyl β-D-1-thiogalactopyranoside (IPTG) once the culture reaches log-phase growth. The competency of BL21 cells is somewhat less than that of other bacterial strains; thus, to obtain a sufficient number of colonies, first amplifying libraries in a high competency strain may be necessary before transforming to BL21. BL21 also shows leaky expression of the protein, which may be a disadvantage if a toxic protein is being expressed. If leaky expression occurs, modified strains such as BL21(DE3)pLysS (Thermo Fisher) are available. The pLysS strain has the added advantage of being able to lyse the cells by repeated freeze-thaw cycles because of the lysogenic enzymes released during each cycle. However, for our purposes, leaky expression is an advantage because IPTG is also somewhat toxic to cells, and with leaky expression, IPTG is not needed at all. Once the bacteria reaches log-phase growth, cultures are simply grown for a long time (72–96 h) at a lower temperature (18 °C), which provides sufficient protein for screening or purification purposes. In addition, leaky expression is useful for colony selection subjected to screening.

Candidate colonies can be derived from libraries of variants grown on one or several agar plates, depending on the size of the library. If selection pressure can be applied at this step, the throughput of the screening will greatly increase. For example, iGluSnFR is a Glu sensor with increased brightness in the presence of Glu. Given that Glu is in the growth medium, colonies could be selected under fluorescent illumination based on their brightness. In this way, thousands of colonies can be screened on a single agar plate in a single step. Not all libraries are amenable to such screening, and in that case, colonies can be picked at random. Selected colonies can then be grown in 1 mL of culture medium in 96-well format deep-well plates. Cultures can be grown as above, first at 37 °C and then at 18 °C, until the desired protein production level is reached (72 h).

When screening, obtaining a quick, reliable, quantifiable readout of the performance of each variant is necessary. Given that the only relevant output of our Glu sensor is its fluorescence upon Glu binding, we test our variants in a simple fluorescence assay with and without Glu. $\Delta F/F$ can then be calculated from these values. Bacterial colonies can be pelleted, washed, and lysed using B-PER Complete (Thermo Fisher). The cell lysate is transferred to a 96-well plate with an optically clear bottom and read on a fluorescent plate reader (Tecan). Reading the same wells both before and after ligand addition is important to control for pipetting-error differences between wells. Testing control wells with no ligand added is also important to control for differences between reads. Top-scoring variants from each plate are regrown and retested as purified protein with multiple concentrations of ligand to confirm the improved performance. Only variants with the best fold-change in fluorescence are then promoted to the next round of evolution.

2.3.2 Photophysical Characterization

After initial screening by expressing the library variants in *E. coli* and measuring changes in fluorescence in the presence and absence of ligands in the lysate, the lead variants will be further purified and subjected to systematic photophysical characterization, under both 1- and 2-photon illumination, as well as ligand-binding specificity measurement. Sensors that perform well under one-photon (1P) excitation do not always translate to good probes for in vivo experiments. One issue that arises is that the 1P molar extinction coefficient of a fluorophore frequently does not serve as a good predictor of 2-photon (2P) cross-section [83]. Testing the brightness of any candidate sensors under 2P excitation becomes necessary to benchmark candidate sensors. We follow methods modified from Makarov et al. and Drobizhev et al. [83, 84] for determining fluorescence lifetime, quantum yield, and 2P cross section.

Fluorescence lifetime measurements can be taken on a synchroscan streak camera (Hamamatsu). Excitation can be performed using the vertically-polarized second harmonic of a Ti:sapphire oscillator (Coherent). Resultant fluorescence can then be collected at 90° relative to the excitation light path and focused onto the streak camera slit using an appropriate objective. Scattered excitation

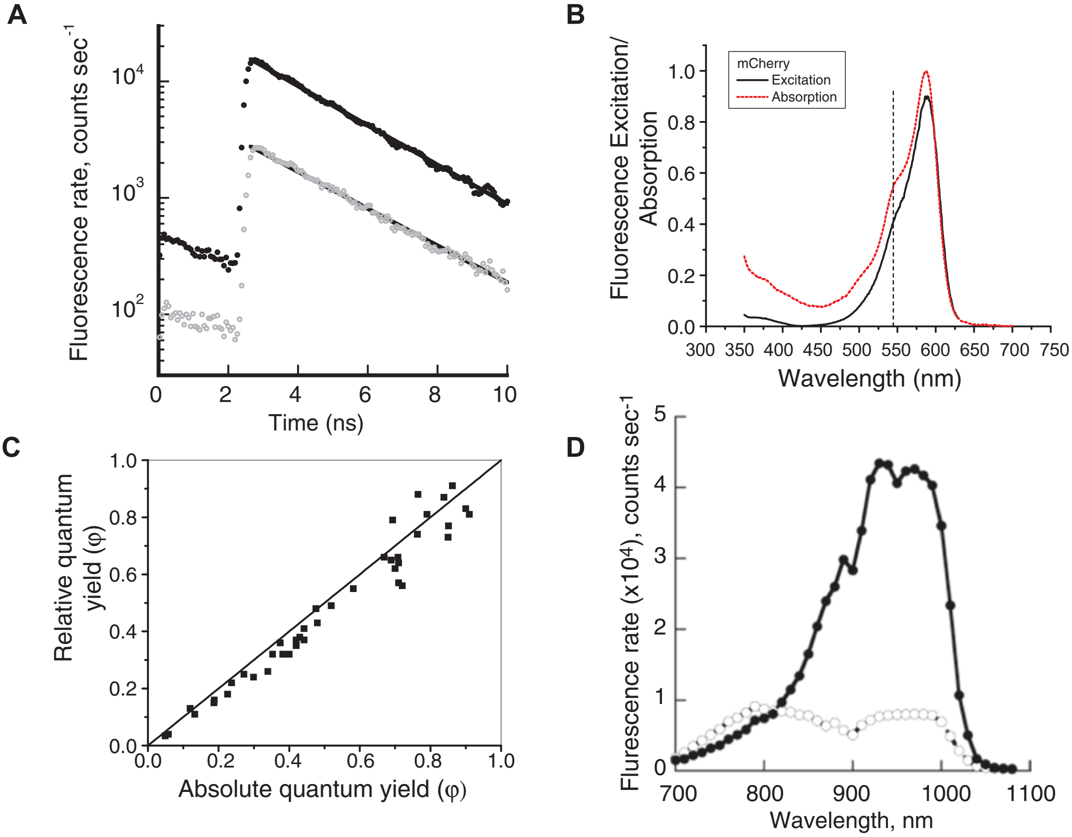

Fig. 5 Determination of the 2-photon cross section of fluorescent protein-based sensors. (**a**) Calculation of the fluorescence lifetime of iGluSnFR in both the apo- (*lower trace*) and bound (*upper trace*) states. (**b**) Graphical description of the normalization procedure used to calculate optical density. In this case, the excitation spectrum of the red fluorescent protein mCherry is normalized to the absorption spectrum of the same sample. (**c**) Scatterplot demonstrating that use of the relative method for determination of quantum yield of proteins leads to systematically lower values than use of the absolute method. Each point indicates values obtained for a single protein. (**d**) Two photon excitation spectra of iGluSnFR in the apo- (*white*) and bound (*black*) states. Reproduced with permission from Marvin et al. (2013) [54] (**a**, **d**), Drobizhev et al. (2009) [100] (**b**), and Drobizhev et al. (2011) [83] (**c**)

photons should be excluded from the detector by utilizing a short-pass filter inserted into the detection light path before the streak camera slit. For Glu sensors, fluorescence decay values should be determined for both apo and bound conformations. For iGluSnFR itself, these values are mono-exponential with a decay constant of around 2.5 ns in each conformation (Fig. 5a) [54]. For sensor variants, a log-linear plot of the photon counts over time will be fit by a line if decay is mono-exponential. The fluorescence time constant can then be fit as a simple exponential decay (Fig. 5a). If the resultant line is not satisfactorily fit by a line, it is likely that more than a single time constant controls the fluorescence lifetime.

In such an instance, the superposition of two (or potentially more) exponential decay processes may serve to better describe the kinetics of fluorescence decay.

Fluorescence quantum yield can be measured either relative to a standard sample or in absolute terms. For determining relative quantum yield, standards with spectral properties that roughly match the properties of the tested sensor variant should be used. For example, sensors with spectral properties similar to iGluSnFR can be compared to Fluorescein in an alkaline (pH 11) solution. Red-shifted sensor variants can be compared with Rhodamine B in methanol, or tested against Rhodamine 6G in ethanol. Fluorescence emission and excitation spectra of purified proteins and reference fluorophores are measured on a luminescence spectrometer (PerkinElmer). Fluorescence spectra are corrected for changes to illumination intensity and detection sensitivity at different wavelengths. Corrected spectra of the sample, $F(\lambda)$, and the reference, $F_R(\lambda)$, can then be integrated over the wavelength range and normalized by optical density of the sample at the excitation wavelength, $\mathrm{OD}(\lambda_{\mathrm{exc}})$, and for the reference, $\mathrm{OD}_R(\lambda_{\mathrm{exc}})$. In each case, keeping the maximum OD low (<0.07) is important to avoid concentration-dependent filtering effects. Note that for fluorescent proteins, calculating OD from the measured absorption spectrum introduces artifact as scattering, and absorption by immature fluorophores contribute strongly at lower wavelengths. Therefore, to approximate the OD for our protein-based sensors, we use the emission spectrum values normalized such that the long wavelength edge overlaps the absorption spectrum (Fig. 5b). By so doing, we isolate that region of the spectra where contributions from scattering and immature fluorophore absorption are minimized. One can then use the value of the normalized excitation spectrum at λ_{exc} as the $\mathrm{OD}(\lambda_{\mathrm{exc}})$. Finally, the fluorescence quantum yield of the sensor, ϕ, can be calculated from the reference quantum yield, ϕ_R, as:

$$\phi = \frac{\mathrm{OD}_R\left(\lambda_{\mathrm{exc}}\right) n^2 \int_0^\infty F\left(\lambda\right) \mathrm{d}\lambda}{\mathrm{OD}\left(\lambda_{\mathrm{exc}}\right) n_R^2 \int_0^\infty F_R\left(\lambda\right) \mathrm{d}\lambda} \phi_R$$

where n and n_R are the refractive indices of the protein and reference solutions, respectively.

Absolute quantum yield values can be calculated by making photon measurements using an integrating sphere device (Hamamatsu). Using this method, all scattered photons that are not absorbed by the sample can be counted, allowing direct experimental access to the number of photons actually absorbed by the sample. Quantum yield is then simply the number of photons emitted divided by the number absorbed by the sample. This method is preferable because it has been shown that the relative method systematically underestimates the true fluorescent quantum yield, presumably due to unaccounted-for scattering contribution to the measurement of OD(λ_{exc}) [83] (Fig. 5c).

For methods developed by Makarov et al., a necessary step in calculating the 2P cross section is determination of the extinction coefficient, ε_{m}. This calculation can be made using an all-optical approach, which obviates the need for making exact measurements of mature fluorophore concentration. Specifically, the fluorescence lifetime, τ, and quantum yield, φ, which do not depend on knowledge of mature fluorophore concentration, can be related directly to radiative lifetime as $\tau_{\mathrm{R}} = {}^{\tau}\!/_{\phi}$. This relationship, along with data taken to determine the fluorescent quantum yield, allows recovery of ε_{m} by a rearrangement of the Strickler-Berg equation, such that:

$$\varepsilon_{\mathrm{m}} = 3.47\times10^{8}\,\frac{\tilde{\nu}_{\mathrm{f}}^{-3}}{n^{2}\int\frac{u(\tilde{\nu})\mathrm{d}\tilde{\nu}}{\tilde{\nu}}}\,\frac{\phi}{\tau}$$

where n is the refractive index of the medium and $u\left(\tilde{\nu}\right)$ is the absorption line-shape function,

$u\left(\tilde{\nu}\right) = {}^{\varepsilon\left(\tilde{\nu}\right)}\!\Big/_{\varepsilon_{\mathrm{m}}}$, and $\tilde{\nu}_{\mathrm{f}}^{-3}$ is the temporal average of the inverse cubic frequency of fluorescence found from the corrected fluorescence spectrum $F\left(\tilde{\nu}\right)$ by:

$$\tilde{\nu}_{\mathrm{f}}^{-3-1} = \int F(\tilde{\nu})\mathrm{d}\tilde{\nu}\Bigg/\int\frac{F(\tilde{\nu})\mathrm{d}\tilde{\nu}}{\tilde{\nu}^{3}}$$

Finally, the 2P absorption cross section (2PA) can be derived using the values of fluorescence lifetime τ, and the extinction coeffiecient ε_{m}. To determine this quantity, we excite samples with a Ti:sapphire femtosecond oscillator (Coherent), pumped by a constant-wavelength, frequency-doubled Nd:YAG laser (Coherent); a 1 kHz repetition rate Ti:Sapphire femtosecond regenerative amplifier (Coherent); and an optical parametric amplifier, OPA (Quantronix), whose output signal or idler is continuously tunable from 1100 to 1600 nm or 1600 to 2200 nm respectively. We use the second harmonic of the signal for 2P excitation in the λ_{exc} = 550–790 region, the second harmonic of the idler in the 790–1100 nm region, and the fundamental signal in the 1100–1400 nm region. The OPA output signal pulse energy is 100–250 μJ (10–40 μJ after frequency doubling), and the pulse duration is 70–120 fs. All 2PA are then determined relative to a set of well-characterized standards [84] to correct spectral variations in the excitation source. Additionally, all fluorescence measurements should be checked to ensure a quadratic relationship to input excitation intensity to exclude artifacts such as linear absorption of photons within the 1P absorption spectrum. The 2PA cross-section of the sample, σ_2, can then be calculated from the reference value, $\sigma_{2,\mathrm{R}}$, as:

$$\sigma_2 = \frac{F_2\left(\lambda_{\mathrm{reg}}\right) C_{\mathrm{R}} \eta_{\mathrm{R}}\left(\lambda_{\mathrm{reg}}\right)}{F_{2,\mathrm{R}}\left(\lambda_{\mathrm{reg}}\right) C \eta\left(\lambda_{\mathrm{reg}}\right)} \sigma_{2,\mathrm{R}}$$

where λ_{reg} is the registration wavelength at which sample and reference values of 2P excited fluorescence, F_2, are taken; C gives the concentration; and η is the differential quantum yield. For all variables, the R subscript denotes values pertaining to the reference standard. Concentration for sample and reference is then calculated by Beer's Law as $C = {}^{\mathrm{OD}_2}\!/_{\varepsilon_{\mathrm{m}} l}$. In this equation, l denotes the cuvette path length, while OD_2 denotes optical density in its spectral maximum. Differential quantum yield of the sample can then be calculated as $\eta\left(\lambda_{\mathrm{reg}}\right) = {}^{F_2\left(\lambda_{\mathrm{reg}}\right)}\!/_{\mathrm{OD}_{\mathrm{abs}}}$, where $\mathrm{OD}_{\mathrm{abs}}$ is calculated for the determination of fluorescence quantum yield of the sample. σ_2 values can be obtained at several points within the 2PA spectrum of the sample. The 2PA spectrum can then be calibrated along its length based on the obtained values of σ_2 (Fig. 5d).

2.4 Microscopes and Imaging Stages

For imaging of cell cultures (heterologous and primary), we use an inverted Zeiss 710 laser scanning confocal microscope equipped with laser lines at 405, 458, 488, 514, 561, and 633 nm. A variety of stage adapters are required to accommodate the different culture systems we use. One stage-adapter system we have found to be particularly useful is an SA-20KZ-AL stage adapter (Warner Instruments, 64-0297) fitted with a QE-1 platform (Warner Instruments, 64-0375). This system accommodates inserts of different sizes, allowing mechanically stable recordings from a variety of culture glassware. In instances where spatial resolution is not paramount, we use a Plan-Apochromat 20×/0.8 NA objective lens (Zeiss, 440640-9903) with the confocal pinhole open to its greatest extent. For higher spatial resolution imaging, for example, when signals near the cell membrane are of interest, we use a Plan-Apochromat 63×/1.4 NA objective lens (Zeiss, 440762-9904) with the pinhole restricted so that the point-spread function of the excitation light through the selected objective passes approximately 1 Airy Disk (i.e., 1 Airy Unit). As a brief aside, Airy unit calculation is made from excitation wavelength as a matter of convenience. This value can be more precisely calculated based on the peak of the emitted fluorescence. This difference can become significant when the imaged fluorophores exhibit a large Stoke's shift. Temporal precision is especially important when imaging iGluSnFR and variants with comparably fast kinetics. For example, fluorescence transients due to spontaneous activity in dissociated neurons are only well resolved at frame rates above 60 Hz, well above the typical 512 × 512 frame rates for our system. With our scanning laser system, tradeoffs can be made between the amount of spatial information collected and temporal precision. For instance, recordings taken at the lowest magnification (0.6×) at the Nyquist limit for resolution for the 63× objective (2316 × 2316) require ~7 s for acquisition of a single image but provide exquisite spatial detail over an extended area (~230 μm). At the other extreme, single-pixel scans can be completed in as little as a few microseconds but provide essentially no spatial information.

Imaging at depth in intact, living animals, particularly in highly scattering mammalian brain tissue, requires 2P microscopy. To test sensors in this imaging modality, we use a SliceScope (Scientifica) outfitted with a resonant (8 kHz) galvo scan head, one gallinium arsenide phosphide (GaAsP) photo-multiplier tube (PMT; Scientifica, S-MDU-PMT-50-65), one conventional PMT (Scientifica, S-MDU-PMT-45), and a Chameleon Ultra II mode-locked Ti:sapphire tunable laser (680–1080 nm; Coherent). Our system is therefore capable of scanning a 512 × 512-pixel image at a rate of ~30 Hz, allowing a dwell time of about 90 ns at each pixel. The image size can thus be reduced along the galvo-scanned axis for a linear decrease in image acquisition time. Indeed, given the fast kinetics of iGluSnFR, an acquisition rate exceeding 100 Hz may be desirable, depending on the speed of the imaged Glu transients themselves. In terms of spatial precision, with our 40× objective, resolution exceeding fine, subcellular neuronal features, such as axons and dendritic spine heads, is easily achieved. Finally, a two-PMT system allows for multiplex imaging of green and red fluorophores. Note, however, that care must be taken to ensure that a single excitation wavelength can effectively drive fluorophores of each color if real-time multiplexing is desirable; otherwise, images can be taken at different excitation wavelengths (a process requiring at least several seconds) and combined offline.

2.5 Imaging-Sensor Variants Expressed in Immortalized Cell Lines

Bacteria-based testing allows rapid screening of libraries of sizes ranging from 10^3–10^5 variants depending on the specifics of the method used. However, protein folding, mature protein localization, maturation temperature, and a host of other differences between bacterial and vertebrate physiology mean that performance in *E. coli* does not necessarily predict performance in mammalian systems. As a middle point between in vitro and in vivo preparations, we used mammalian HEK293 cells and rat hippocampal dissociated neuronal culture to characterize the sensor's intrinsic properties, such as expression level, affinity, and sensitivity to perfused Glu or action potential-triggered Glu release (Fig. 6).

2.5.1 Preparing HEK293T Cells for Imaging Experiments

When testing candidate probes in heterologous cells, we use HEK293T cells (Thermo Fisher, R70007). Generally, these cells can be maintained with a standard culture medium composed of Dulbecco's modified Eagle's medium (Thermo Fisher, 11995-065) supplemented with 10% v/v fetal bovine serum (Thermo Fisher, 10437028) and PenStrep at 50 U/mL (Thermo Fisher, 15070063). Because these cells are quite hardy, we flash freeze them as stocks of one million cells per 1 mL aliquot in the standard culture medium, supplemented with 10% v/v dimethyl sulfoxide (Sigma, D8418). To prepare cells for imaging, we plate onto 12 mm round glass coverslips (Thermo Fisher, 12-545-81). Critically, any culture dish used must have #1.5 glass to be compatible with confocal objectives. When the cells are ~60% confluent, we transfect using Effectene (Qiagen, 301425) and miniprep plasmid DNA (Qiagen, 27106), per the manufacturer's recommended protocols. Depending on the specifics of the promoter and construct, imaging can usually be performed 24–48 h after transfection. Typically, we use a CMV or CAG promoter for expression in HEK293T, since both rapidly (within 12 h post transfection depending on the construct) drive high levels of sensor expression.

2.5.2 Deriving Sensor-Apparent K_d on HEK293T Cells

While screening in *E. coli* serves as a high-throughput front-end screen in sensor development, differences in probe performance are possible when expressed in a mammalian system. For example, as the characterization of iGluSnFR moved from purified *E. coli* lysates to surface expression on mammalian cells, the apparent K_d was notably reduced by greater than an order of magnitude [54]. Such discrepancies demand testing in systems that more closely reflect the eventual system of study.

Characterization on HEK293T cells offers a medium throughput step in determining suitability of a particular candidate sensor for its final application (Fig. 6a and b). It is possible to use this system to easily determine the apparent K_d of a Glu sensor when expressed at cell surface. Within the context of this process, determining the $\Delta F/F$ of the candidate sensor is also possible.

To determine apparent K_d of the sensor, we image sensors transfected into HEK293T cells as described in Sect. 2.5.1. The day of the experiment, we make a $\log_2$ series of Glu dissolved in HEPES-buffered (20 mmol/L) Hanks' balanced salt solution (HHBSS), with pH adjusted to 7.4. The concentrations are chosen to match the expected affinity of the sensor, so iGluSnFR concentrations will range from high nanomolar to several hundred micromolar. We then gently wash the cells three times with HHBSS and mount the coverslip to the stage adapter, which is then affixed to the Zeiss 710 stage. To minimize motion artifact (axial or lateral

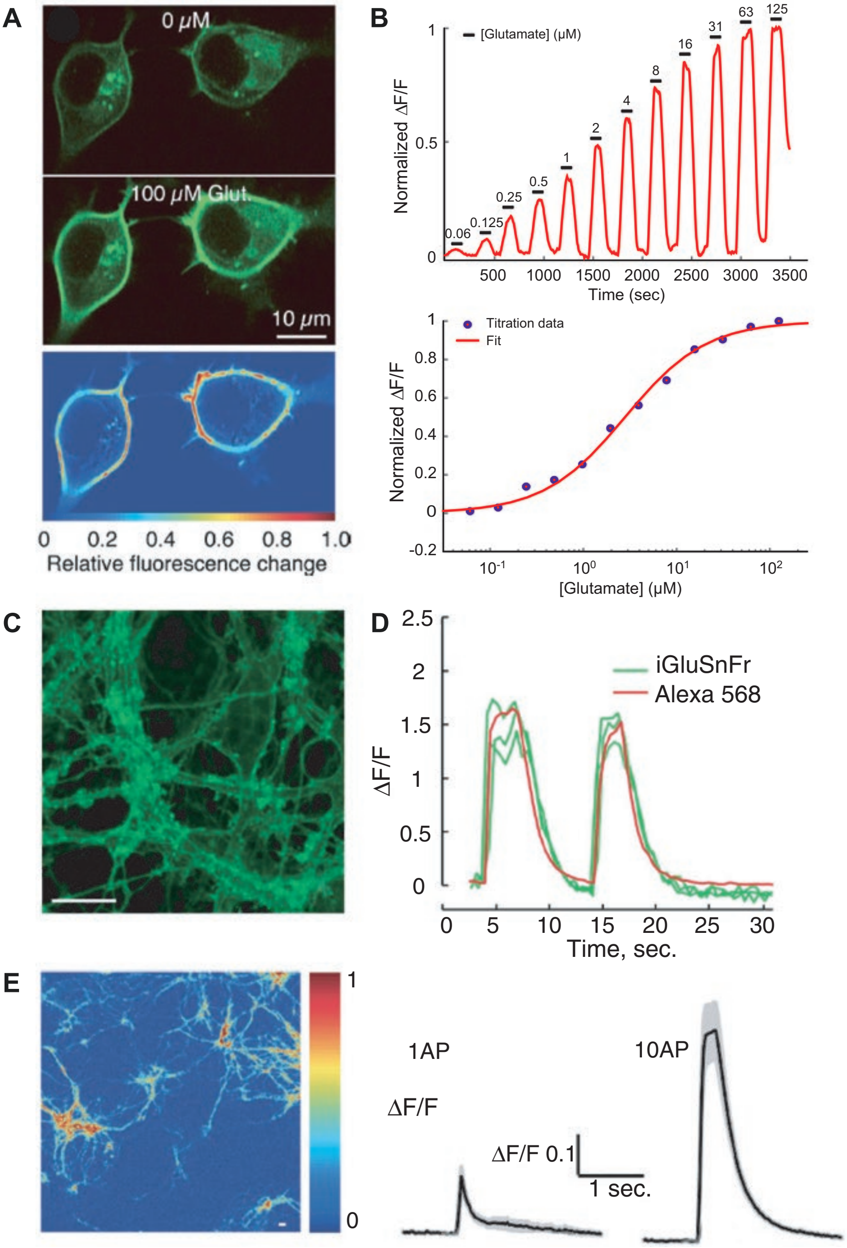

Fig. 6 (**a**) Expression of iGluSnFR on HEK293 cells. (**b**) Perfusion of different Glu concentrations on HEK293 cells to determine the K_d (4 μmol/L). Measurements are from a single ROI. (**c**) Dissociated hippocampal neurons infected with AAV.hSynapsin.iGluSnFR. (**d**) Response of neurons to "puffs" of Glu/AlexaFluor 568 solution. (**e**) Response of neurons to electrical field stimulation. Reproduced with permission from Marvin et al. (2013) [54]. Scale bar = 10 μm. Reproduced with permission from Marvin et al. (2013) [54] (**a**,**c**-**e**)

from cell movement), we image using the 20× objective with the confocal pinhole opened as wide as possible. HHBSS is then perfused onto the chamber using a peristaltic pump set to a perfusion rate of about 1.5 mL/min. We then alternate between washing with HHBSS and applying the Glu titration from the lowest to highest concentration values. For each concentration and wash, we allow 3 min for full equilibration of the stage concentration. During this procedure, we capture images at a rate of one per 10 s with a 512 × 512 pixel size and pixel dwell of around 6 μs.

Data is processed by hand-drawing regions of interest (ROIs) over cells within the image that are assessed as having moved very little by their average intensity projection along the time axis. Averages within these ROIs are taken point-wise following the equation $\frac{\Delta F}{F} = \frac{F - F_0}{F_0}$. Here, F_0 is the background-subtracted average fluorescence during the period prior to the first Glu application, and F is a vector of background-subtracted mean intensities for each time point. To calculate the apparent K_d, we fit the peaks in the resultant traces to a single binding-site isotherm using custom Matlab (Mathworks) routines. $\Delta F/F$ can also be extracted as the maximum point in the curve.

2.6 Imaging-Sensor Variants Expressed in Primary Cell Lines

While immortalized cell lines offer a convenient way to test sensor variants, they lack aspects of neuronal signaling, including exocytotic release of Glu. As a final test before packaging candidate sensors for expression in intact mammalian preparations, we characterize performance in dissociated neuronal culture (Fig. 6c–e).

2.6.1 Preparing Primary Neuronal Cultures

For imaging experiments that require primary dissociated cells, we use hippocampal cells derived from E18 Sprague-Dawley pups (Charles River). One day prior to the dissection, we coat culture dishes (35 mm Petri dishes) with 14 mm #1.5 glass window (MatTek, P35G-0.170-14-C) with a sufficient volume of 10 μg/mL laminin (Sigma, L2020) and 10 μg/mL poly-DL ornithine (Sigma, P0421) to cover the area to which the cells will be seeded. The coating is kept on the culture dishes overnight and then rinsed four times with sterile deionized water.

On the day of the dissection, the pregnant female is deeply anesthetized by isoflurane (Henry Schein, 50562-1) in an induction chamber. We then cervically dislocate the animal and perform a Cesarean section to remove the uterus. Individual pups are removed from the uterus and rapidly decapitated. The heads are placed in sterile HBSS (Thermo Fisher, 14175103) in a 10 cm Petri dish. Heads are then stabilized by poking the tips of Dumont #7 forceps (Fine Science Tools, 11274-20) through the ocular sockets, and the brains are removed by cutting caudal to rostral along the sagittal suture using 3 mm angled Vannas scissors (Fine Science Tools, 15000-00). The brains are removed with a microspatula (Thermo Fisher, 21-401-10) and placed into a 35 mm Petri dish containing HBSS where they are stabilized for dissection by impaling the cerebellum with Dumont #5 forceps (Fine Science Tools, 11251-10).

We perform the hippocampal dissection using a scalpel (Fine Science Tools, 10035-15) to delicately peel back one hemisphere of cortex, gently pulling with the forceps to remove the meninges. We stabilize the hippocampus by placing the forceps onto the surrounding cortex, and then cut away the cortical tissue. Isolated hippocampi are transferred to a 15 mL conical tube containing 2 mL of 0.05% trypsin (Thermo Fisher, 25300120) and placed into a cell culture incubator at 35 °C for 15 min. Following the incubation period, the trypsin is inactivated by adding 10 mL of NeuroBasal (NB; Thermo Fisher, 21103049) supplemented by 2% B27 (Thermo Fisher, 17504044) and 5% fetal bovine serum (FBS). Hippocampi are then transferred to a 15 mL conical tube containing 5 mL HBSS where the tissue is triturated by suctioning into and out of a constricted (~500 μm diameter) Pasteur pipette about 15 times, or until there are no large pieces of tissue remaining. We then allow the debris to settle for a few minutes and transfer the cell-containing supernatant to an empty 15 mL conical tube. Finally, the supernatant is centrifuged at 500 rcf for 3–5 min at room temperature, and the pellet is resuspended in sufficient NB + B27 + FBS for seeding onto the prepared culture dishes.

Cells are allowed to grow undisturbed for ~4 days or until astrocyte proliferation is sufficient to produce a nearly confluent monolayer. At this point, we perform a half change of the medium with fresh media further supplemented by 10 μmol/L 5-fluoro-2′-deoxyuridine (FUDR, Sigma, F0503) final concentration. Neurons so-derived can be transfected using the calcium phosphate method (Thermo Fisher, K278001), per the manufacturer's instructions, between 5 and 10 days in culture. Because primary cells are more sensitive to culture conditions, we generally use an endotoxin-free DNA preparation method such as the ZR plasmid miniprep kit (Zymo Research, D4015). In addition, CMV and CAG promoters drive expression of the sensor in nonneuronal cells, so for neuronal transfections, we instead use the hSynapsin promoter, which results in neuron-specific sensor expression.

2.6.2 Determining Sensor Action-Potential Sensitivity

For these experiments, we first wash the cells three times by HHBSS. The MatTek culture dish is then placed into the stage adapter and affixed to the Zeiss 710 stage, after which we attach electrophysiology insert RC-37FS (Warner Instruments) above the cells. While placing the RC-37FS above the cells, care must be taken to position the insert slowly and at an angle to avoid applying excessive positive pressure down onto the coverslip. We then drive an isolated electrical current controlled by Ephus software (Vidrio Technologies) across the stage to stimulate action potentials in the cultured neurons. Stimuli are delivered as 1 V square-wave pulses with 1 ms duration at 30 Hz. These stimuli drive simultaneous action-potential activation across the stage, resulting in extensive extra-synaptic spillover of Glu [53]. Because the extra-synaptic

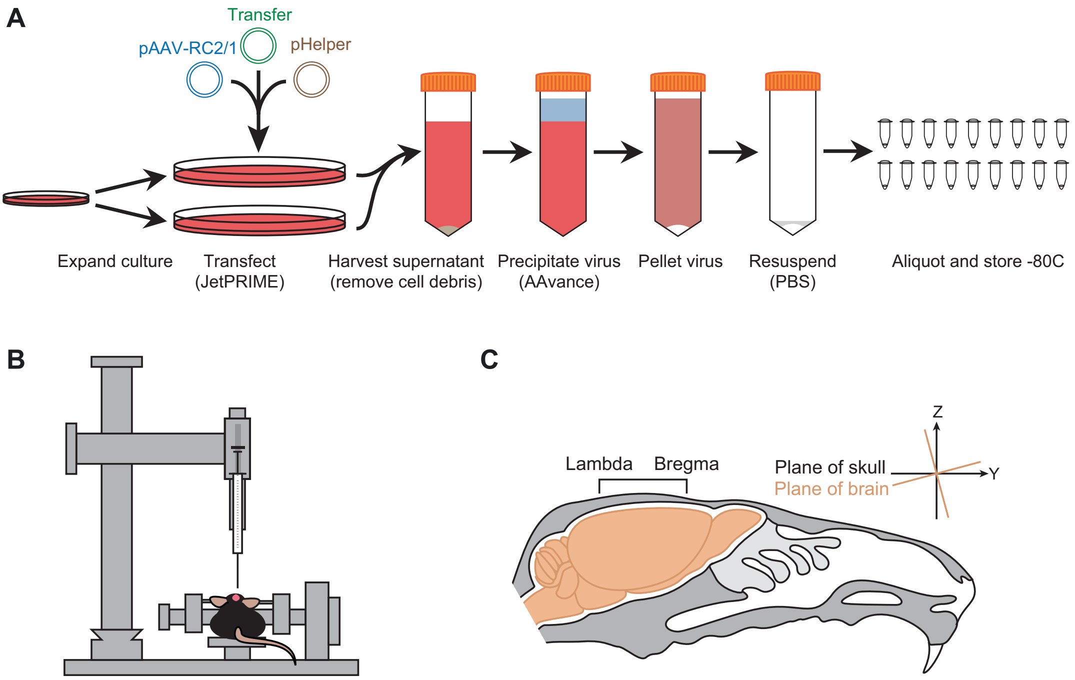
A
Transfer
pAAV-RC2/1
pHelper
Expand culture
Transfect (JetPRIME)
Harvest supernatant (remove cell debris)
Precipitate virus (AAvance)
Pellet virus
Resuspend (PBS)
Aliquot and store -80C
B
C
Lambda
Bregma
Plane of skull
Plane of brain
Z
Y

Fig. 7 (**a**) Protocol for making adeno-associated virus (AAV). (**b**) Stereotaxic setup for injecting virus into a mouse brain. (**c**) Position of mouse brain inside the skull, and relative to suture landmarks

spillover is more spatially and temporally extensive than synaptic Glu signaling, we are able to image these events at <20 Hz and capture the shape of the resultant fluorescence waveform. However, it is also possible to capture spontaneous synaptic and extra-synaptic activation by increasing the frame rate to ~60–100 Hz (Fig. 6c).

2.7 *In Vivo* Characterization of Sensor Variants

Sensor characterization is not complete without expression within the animal system of interest. Here, we discuss procedures for transduction of cells within the intact mouse brain and in vivo imaging.

2.7.1 Virus Preparation

For in vivo transduction, particularly in mammalian experimental systems, recombinant adeno-associated virus (rAAV) has become the vector of choice. In large part, this preference has come about because rAAV does not incorporate into the host-cell genome (preventing possible insertional mutagenesis); drives high, relatively constant levels of the transgene payload; and can be produced at very high titers (10^{12} virion/mL is not an uncommon benchmark) relatively inexpensively (Fig. 7a). As such, it has the potential to serve sensor workflows in the final in vivo phases of testing. For the interested researcher, the only potential caveat is that common academic viral cores, such as those housed at the Universities at Pennsylvania and North Carolina Chapel Hill, require a roughly $2000 USD investment per custom vector packaged in rAAV.

Fortunately, recent years have seen the development of much more cost-effective production methods that can be performed with equipment common in many laboratories. Our particular workflow typically produces virus at 5×10^{12} genomic count (GC; i.e., viral genome counts) per mL, with a total yield of around 5×10^{11} GC at a cost of under $200 USD.

For a single rAAV batch, we plate 10^6 reconstituted AAV293 cells (Agilent Technologies, 240073) onto a 10 cm tissue culture dish using 10 mL of the culture medium described in Sect. 2.5.1. Once these cells have grown to ~60% confluency (typically after 1–2 days), we split these cells onto two 15 cm tissue culture dishes in 20 mL culture medium. After waiting for the cells to reach 50–80% confluency, we change to a fresh 20 mL of culture medium. Next, we perform a transfection using jetPRIME transfection reagent (Polyplus, 114-15). To prepare the transfection complex, we combine 2 mL of the jetPRIME buffer with the jetPRIME reagent and the transfer plasmid, along with helper plasmids pHelper and pAAV-RC2/1 (Agilent, 240071), into an appropriate conical tube at a ratio of 80 μL:17 μg:14.5 μg:8.4 μg. The complete transfection mixture is then applied, 1 mL per tissue culture dish, per the manufacturer's recommendations. After a 72-h incubation period, we collect the supernatant from both plates into a 50 mL conical tube, pellet out any cell debris, add 10 mL AAVanced Concentration Reagent (Systems Bioscience, AAV100A-1), and concentrate the virus per the manufacturer's recommendations.

Critically, it should be noted that different rAAV serotypes have been shown to release from host production cells with different efficiencies [85]. Our production method ensures relatively pure virus by harvesting only from the culture supernatant rather than lysed cells. Therefore, serotypes that do not localize to the supernatant are not suited to our process. The propensity to remain in production cells rather than be released to the supernatant is thought to be driven primarily by the relative affinity of the capsid protein for heparin. Thus, RC helper plasmids containing, for example, the serotype 2 *cap* gene should be avoided because the resultant protein has a high affinity for heparin.

2.7.2 Stereotactic Injection of rAAV

To target the virus to the brain ROI, delivery directly to the brain is necessary because viruses are able to cross the blood–brain barrier only under specific circumstances (Fig. 7b and c). Before surgery, the animal must be anesthetized, which should be confirmed by a toe-pinch test. Common ketamine-based cocktails, such as ketamine/xylazine/acepromazine, do not induce surgical-plane anesthesia, so underdosing and supplementing with an inhaled anesthetic such as isoflurane is preferable. Inhaled anesthetics may also be used without an injectable anesthetic, but must be supplemented with some sort of analgesia during the surgery, such as meloxicam or carprofen, because isoflurane provides no analgesia itself. Topical analgesics, such as lidocaine, are also recommended at the incision site which can be injected subdermally or applied as a jelly to the surface after sterilization of the incision site. Opiate-based analgesics are not recommended before or during the surgery since opiates are respiratory depressants and may cause accidental death during anesthesia. Inhaled anesthetics have the added advantages that the dosing is much easier to adjust during surgery, and they have very fast recovery times (5–10 min). Injectable anesthetics may require several hours before the animal is ambulatory again.

Selection of injection coordinates can be made using a mouse brain atlas such as the one produced by Franklin and Paxinos [86]. Mouse brain atlas coordinates are surprisingly accurate, with only small animal-to-animal variability, particularly for the most common inbred strains, such as C57Bl/6 (Black 6) or 129/SvEv. However, with several inbred mouse strains, the skull is angled relative to the brain; thus, coordinates need to be adjusted to accommodate this tilt. For structures near the surface of the brain, such as the cortex, making any adjustments is not necessary, and surface landmarks such as blood vessels and skull sutures may be used for positioning the needle. However, deeper structures must account for this angle and must also account for any rotation of the skull relative to the manipulating arm of the stereotax. To ensure accurate positioning of the injection needle, it is possible to take measurements from the surface of the skull and use a rotation matrix to recalculate coordinates for drilling and needle insertion (for details, see Note 1).

Once coordinates have been chosen and located relative to the skull surface, a virus is introduced through a small craniotomy, just large enough for the needle to fit through. The needle should be lowered slowly to prevent excess tissue damage and to prevent the tissue from compressing, which would change the location of the target structure. Pulled glass pipettes are thinner and do less damage than steel needles, but cannot reach deeper structures and are at risk of breaking off inside the brain. For shallower structures (0–3 mm), we use glass pipettes, while for deeper structures (3–6 mm), we use 33G steel needles. The virus is then injected slowly (50–100 nL/min) using a high-precision micropump (picospritzer, nanoject, WPI micropump). Waiting a few minutes after the injection is complete allows the virus to diffuse away from the needle tip, lowering the chance of it getting drawn back up the needle track during removal. Remove the needle slowly to minimize tissue damage. After the virus has been delivered, the wound can be closed using either sutures or skin glue (vetbond, dermabond, liquid band-aid). Wound clips are not recommended for the scalp because mice have a tendency to scratch and rip them out.

Stereotaxic surgery can be a time-consuming process and is difficult to master. There are several alternatives, including in utero electroporation, perinatal injection, or tail vein injection. In utero electroporation is a method whereby plasmid is injected directly into the brain of embryos and then the brain is electrically stimulated, either through the uterine wall or using microelectrodes, so that the cells of interest take up the plasmid. This process is not as precise and has a lower survival rate than adult injection, but it is faster and easier to do many animals. Perinatal injection is similar to adult injection, except that the skull is sufficiently soft that the needle can puncture it, and no incision or drilling is necessary. Considerable precision is lost, but speed and facility make it possible to do many more animals. A third option is to package the virus such that it can cross the blood–brain barrier and inject it via the tail vein [87]. This method is quite easy and can theoretically be done at any age; however, the virus will infect most of the brain, so some level of genetic control is recommended. In addition, different packaging plasmids provide slightly different infectivity for different brain regions.

2.7.3 Window and Head Post-Implantation

To view the brain, a craniotomy needs to be performed and a window implanted. This is typically done at the same time as virus injection. The skull should be removed by drilling a doughnut shape larger than the area to be imaged. Drilling causes damage to the brain so any additional drilling should be avoided. The circular piece of skull above the imaging area should be lifted away carefully. The dura can be left intact, and serves as a depth marker during imaging because it displays a stereotyped autofluorescence. Again, avoid damaging the brain in the imaging area. At this point, the remaining surface of the skull should be scuffed up using sharp forceps or another abrasive tool. This creates additional surface area for adhering the cement to the skull later. A circular glass coverslip is then lowered and held in place just above the brain and barely touching the highest point. The angle of the coverslip should be match the most optimal viewing angle for the brain region to be imaged. It is also possible to install a small prism in order to change the imaging angle for access to non-surface structures [88, 89]. Low melting point agarose is then used to fill in the remaining space between the brain and the coverslip. Avoid air bubbles when filling in the gaps. Then the skull should be covered with a thin layer of crazy glue in order to improve the bond of the cement. Only a small amount of glue should be on the agarose and coverslip. Then a custom headpost can be fitted around the coverslip. The headpost should be large enough to accommodate the desired objective, and have protrusions that can be clamped into the headstage to reduce motion artifacts during imaging. The coverslip and headpost are then secured to the skull with black pigmented dental cement. The black pigment helps to reduce light pollution during imaging, particularly for experiments involving visual stimuli. The cement will harden within 30 min, and will fully cure within 24 h. The skin should be closed around the cement to cover any exposed areas of the skull using skin glue, to prevent infection.

2.7.4 Head Mounting and In Vivo Imaging

To collect usable data from the sensor, it is important to obtain a stable image, which be achieved by clamping the head under the microscope using the headpost installed during surgery. Anesthesia is not necessary at this step, but may be used if preferred. The headpost should fit reliably into the clamping mechanism such that individual cells can be identified and imaged multiple times during repeated imaging sessions. The clamp should also be solid enough to overcome any forces created by the animal. One option is to anesthetize the animal during imaging; however, anesthesia may not be compatible with the behavioral paradigm, and different forms of anesthesia may alter the activity of different brain regions. For awake recordings, the animal should be mounted on a moveable surface to enable walking and running, such as a treadmill, a rotating disc, a suspended ball [90], or a mobile homecage [91]. Techniques involving restraint are not recommended because this is highly stressful for the animal, which may alter the results of the experiment, and causes unnecessary duress. If a restraint method is desired, the animal must be well habituated to the restraint, a process that requires 8–10 days of daily restraint, and may be supplemented with regular rewards [92, 93]. Obviously, the more natural the motion (suspended ball or mobile homecage), the less stressful the experiment will be for the animal. We use a suspended ball because of its lower cost of installation. Several habituation sessions may be required before performing the actual experiment. In addition, adding a shield may be necessary to protect the objective from the motion of the animal's tail, as well as stray light sources, such as those introduced by application of visual stimuli.

Even if all forces are eliminated from the animal's walking and running, the animal's heartbeat, breathing, and whisking will still create motion artifacts. Motion in the x–y plane can be easily eliminated by reregistering the images before analysis [94]. Artifacts in the z-plane are more problematic in that they change which objects are within the focal plane. Some solutions for mitigating this issue involve real-time adjustments of the focal plane or broadening the focus so that fluctuations along the axial direction do not affect the image [95].

A properly prepared animal will allow assessment of sensor function in intact tissue. We have successfully imaged spontaneous Glu transients in apical dendrites of cortical pyramidal cells in anesthetized, as well as awake, behaving rodents. In our hands, this spontaneous Glu release was modified during certain behavioral paradigms, as well as under pharmacological manipulation [54] (Fig. 8). Following these and similar procedures, it will be possible

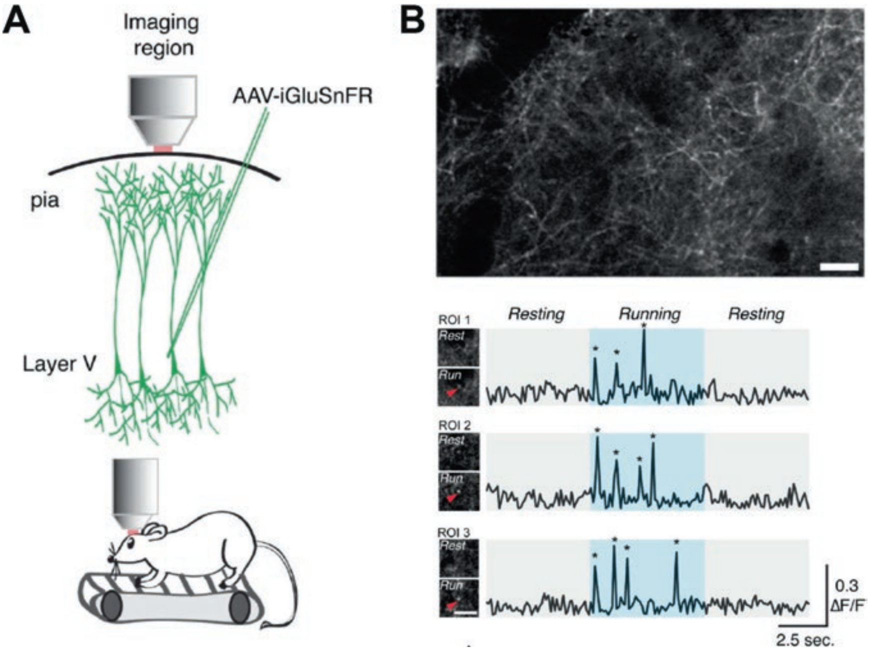

Fig. 8 (**a**) Schematic illustrating experimental approach for injection of AAV.hSynapsin.iGluSnFR into layer V of primary motor cortex for in vivo transcranial two-photon microscopy. (**b**). Two-photon image of low-density infection of primary motor cortex (forelimb region) and representative ROIs showing that iGluSnFR signals correlate with onset and offset of locomotion. *, glutamate events. Reproduced with permission from Marvin et al. (2013). Scale bar = 10 μm

to determine whether candidate sensors are able to operate in relevant physiological ranges, in terms of both sensitivity and kinetics, to detect the required Glu transients.

3 Perspective

Despite iGluSnFR's broad success in detecting Glu release in in situ and in vivo preparations, further adjustments to its current attributes may yield additional useful probes. For example, tweaks to iGluSnFR's affinity profile will result in probes that can be used in contexts where iGluSnFR currently functions poorly. Particularly, the apparent cell-surface K_d of 4 μmol/L would suggest that the majority of iGluSnFR localized to the synaptic cleft should be saturated as action potential-evoked Glu transients rise briefly (<10 ms) into the millimolar range [7]. Therefore, a variant with decreased affinity may be able to track synaptic Glu more effectively while excluding signal derived from extra-synaptic Glu. Synaptic signal may be further enhanced by targeting the sensor to the synaptic cleft, reducing nonsynaptic fluorescence sources (see, e.g., [96]). In addition, the kinetics of iGluSnFR can be further optimized for "slow" laser-scanning microscopy. The decay dissociation rate constant allows for an elongation of the fluorescence reporter of the Glu transient, increasing photon budget and resultant SNR. Such elongation can be particularly helpful for SNR when utilizing imaging modalities where frame rates are relatively slow, as in the case of laser-scanning microscopy. For example, 2P laser scanning microscopy provides full field frame rates of tens of hertz, a sampling rate too low to effectively capture the upstroke of a synaptic Glu transient. Therefore, it is essential to develop Glu sensors with slower kinetics that enable large-scale monitoring of transient responses at individual synapses in the living animal.

Additionally, as iGluSnFR is fundamentally a GFP-based sensor, it should be possible to shift its spectral attributes. In particular, a red-shifted variant would be desirable because red light is less scattered in intact tissue [97]. Spectral variants can and should be utilized in conjunction with other tool classes. For example, iGluSnFR could be combined experimentally with the red GECIs from the jRCaMP series [98] or optogenetic actuators with red-shifted action spectra, such as ReaChR [99]. Experimental conditions requiring optogenetic multiplexing with iGluSnFR would find particular benefit in a red-shifted iGluSnFR variant.

To date, how the complex patterns of glutamatergic signaling at multiple synapses interact to drive changes in circuit connectivity remains poorly defined. New types of Glu sensors need to be developed that will permit visualizing the history of neural activity at individual synapses in large fields of view during short behavioral epochs. Broad application of these proposed Glu integrators/sensors would transform the activity of transient synaptic inputs into permanently labeled active synapses, thus enabling access to information mapping neural activity to the structure of the neural circuitry underlying a specific physiological process or behavioral task.

4 Note

1. In many stereotaxic frames, precise control of positioning of landmark coordinates is a difficult task. As an alternative, we have developed a strategy that allows recovery of coordinates rotated from the frame of the mouse head into the reference frame of the stereotax. In this derivation, we assume that the mouse frame does not deviate by more than $\pi/2$ radians in any of the three directions from the stereotax frame.

   Prior to inputting coordinates for determining proper rotation, bregma should be set to the coordinates (0, 0, 0). Once that is accomplished, required inputs include the coordinates of lambda, and two points that lie to 2 mm to the right and left, respectively, of the midpoint of the projection of an imaginary line connecting bregma to lambda onto the horizontal plain. The left and right points can then be sampled two millimeters to the left and right of the line along a line perpendicular to the bregma-lambda projection. We then define variables:

$\vec{\lambda} = [\lambda_1, \lambda_2, \lambda_3]$ is the vector from the bregma to the lambda.

$\vec{R}$ is the vector from bregma to the right sampled point (facing forward along $\vec{\lambda}$ toward bregma).

$\vec{L}$ is the vector from bregma to the left sampled point (facing forward along $\vec{\lambda}$ toward bregma).

$\vec{J} = [J_1, J_2, J_3]$ is the vector $\vec{R} - \vec{L}$.

$\vec{N} = \vec{\lambda} \times \vec{J}$ is a normal vector to the horizontal plane in the mouse head frame.

$\vec{K} = [-\lambda_1\lambda_3, -\lambda_2\lambda_3, \lambda_1^2 + \lambda_2^2]$ is a vector orthogonal to $\vec{\lambda}$. It is in the direction that $\vec{N}$ would be if there were no roll.

$\vec{v}$ will denote the norm of a vector.

θ will denote the angle of yaw; ϕ will denote the angle of pitch; ψ will denote the angle of roll.

Yaw Calculation

$$\theta = \arcsin\left(\frac{\lambda_1}{\sqrt{\lambda_1^2 + \lambda_2^2}}\right)$$

Pitch Calculation

$$\phi = \arcsin\left(\frac{-\lambda_3}{\vec{\lambda}}\right)$$

Roll Calculation

$$\psi = -\operatorname{sgn}(J_3) \cdot \arccos\left(\frac{\vec{K}\ \ \vec{N}}{\vec{K} \ \cdot\ \vec{N}}\right)$$

where $\operatorname{sgn}(J_3)$ is the sign of J_3.

The coordinate transformation from the frame of the mouse's head, $[x, y, z]$ to the frame of the stereotax, $\left[\tilde{x}, \tilde{y}, \tilde{z}\right]$, is as follows:

$$\begin{bmatrix} \cos(\theta) & -\sin(\theta) & 0 \\ \sin(\theta) & \cos(\theta) & 0 \\ 0 & 0 & 1 \end{bmatrix} \cdot \begin{bmatrix} 1 & 0 & 0 \\ 0 & \cos(\phi) & -\sin(\phi) \\ 0 & \sin(\phi) & \cos(\phi) \end{bmatrix} \cdot \begin{bmatrix} \cos(\psi) & 0 & \sin(\psi) \\ 0 & 1 & 0 \\ -\sin(\psi) & 0 & \cos(\psi) \end{bmatrix} \cdot \begin{bmatrix} x \\ y \\ z \end{bmatrix} = \begin{bmatrix} \tilde{x} \\ \tilde{y} \\ \tilde{z} \end{bmatrix}$$

As linear operators it is:

$$\Upsilon(\theta)P(\phi)B(\psi)\vec{x} = \vec{\tilde{x}}$$

The inverse operator taking coordinates in the stereotax frame to the mouse frame is:

$$B(-\psi)P(-\phi)\Upsilon(-\theta)\vec{\tilde{x}} = \vec{x}$$

As an example, we can use these equations to recalculate coordinates for the dorsal lateral geniculate nucleus (dLGN), a brain structure found at ±2.25, −2.30, −2.80 (*x*, *y*, *z* corresponding to mediolateral (ML), anteroposterior (AP), dorsal ventral (DV) directions, respectively). Note that these coordinates have been corrected for the tilt of the skull relative to the brain for our mouse strain (Black 6) as determined by pilot injections. If bregma is set to 0, 0, 0 (*x*, *y*, *z* or ML, AP, ML), and lambda is measured at −0.16, −4.40, −0.64 (*x*, *y*, *z* or ML, AP, ML), then the pitch is calculated to be 8.27° and the yaw is calculated to be −2.08°. We then measure the height of the skull at the points −2.08, −2.13 (left, *x*, *y* or ML, AP) and 1.92, −2.27 (right, *x*, *y* or ML, AP), which are points 2 mm from the center of the line connecting bregma and lambda, and determine that they are −0.45 (*z* or DV) and −0.10 (*z* or DV) respectively. We can now calculate the roll to be −4.95°. Based on this rotation, our corrected drill sites should be at −2.06, −1.77 (left, *x*, *y* or ML, AP) and 2.41, −1.99 (right, *x*, *y* or ML, AP), and we should lower the needle to a depth of −3.28 (*z* or DV) and −2.90 (*z* or DV) respectively.

Acknowledgements

This work is supported by NIH DP2 MH107059 (L.T.), Brain Initiative U01NS090604 (L.T., E.K.U., G.J.B.) and U01NS09058 (R.L.), Rita Allen Foundation (R.L.), Human Frontier Research Program (G.J.B.), and NIH R21NS095325 (B.P.M.). We are grateful for the contributions of Douglas Unger in generating the rotation matrix. We are grateful to Loren Looger, Jonathan Marvin and Philip Borden for their pioneering work in engineering iGluSnFR and critical comments. We also thank Lisa Makhoul for careful reading and discussion of this book chapter.

References

1. Attwell D, Laughlin SB (2001) An energy budget for signaling in the grey matter of the brain. J Cereb Blood Flow Metab 21:1133–1145. doi:10.1097/00004647-200110000-00001
2. Kwon H-B, Sabatini BL (2011) Glutamate induces de novo growth of functional spines in developing cortex. Nature 474:100–104. doi:10.1038/nature09986

3. Lüscher C, Malenka RC (2012) NMDA receptor-dependent long-term potentiation and long-term depression (LTP/LTD). Cold Spring Harb Perspect Biol. doi:10.1101/cshperspect.a005710
4. Volterra A, Liaudet N, Savtchouk I (2014) Astrocyte Ca2+ signalling: an unexpected complexity. Nat Rev Neurosci 15:327–335. doi:10.1038/nrn3725
5. Arundine M, Tymianski M (2004) Molecular mechanisms of glutamate-dependent neurodegeneration in ischemia and traumatic brain injury. Cell Mol Life Sci 61:657–668. doi:10.1007/s00018-003-3319-x
6. Woodroofe N, Amor S (2014) Neuroinflammation and CNS disorders. John Wiley & Sons, West Sussex, UK
7. Clements JD (1996) Transmitter timecourse in the synaptic cleft: its role in central synaptic function. Trends Neurosci 19:163–171. doi:10.1016/S0166-2236(96)10024-2
8. Marcaggi P, Attwell D (2004) Role of glial amino acid transporters in synaptic transmission and brain energetics. Glia 47:217–225. doi:10.1002/glia.20027
9. Ventura R, Harris KM (1999) Three-dimensional relationships between hippocampal synapses and astrocytes. J Neurosci 19:6897–6906
10. Veruki ML, Mørkve SH, Hartveit E (2006) Activation of a presynaptic glutamate transporter regulates synaptic transmission through electrical signaling. Nat Neurosci 9:1388–1396. doi:10.1038/nn1793
11. Moussawi K, Riegel A, Nair S, Kalivas PW (2011) Extracellular glutamate: functional compartments operate in different concentration ranges. Front Syst Neurosci. doi:10.3389/fnsys.2011.00094
12. Ferraguti F, Shigemoto R (2006) Metabotropic glutamate receptors. Cell Tissue Res 326:483–504. doi:10.1007/s00441-006-0266-5
13. Hollmann M, Heinemann S (1994) Cloned glutamate receptors. Annu Rev Neurosci 17:31–108. doi:10.1146/annurev.ne.17.030194.000335
14. Zito K, Scheuss V (2009) NMDA receptor function and physiological modulation. Encyclopedia Neurosci. doi:10.1016/b978-008045046-9.01225-0
15. Conn PJ, Pin JP (1997) Pharmacology and functions of metabotropic glutamate receptors. Annu Rev Pharmacol Toxicol 37:205–237. doi:10.1146/annurev.pharmtox.37.1.205
16. Marcaggi P, Mutoh H, Dimitrov D et al (2009) Optical measurement of mGluR1 conformational changes reveals fast activation, slow deactivation, and sensitization. Proc Natl Acad Sci U S A 106:11388–11393. doi:10.1073/pnas.0901290106
17. Vafabakhsh R, Levitz J, Isacoff EY (2015) Conformational dynamics of a class C G-protein-coupled receptor. Nature 524:497–501. doi:10.1038/nature14679
18. Masugi-Tokita M, Shigemoto R (2007) High-resolution quantitative visualization of glutamate and GABA receptors at central synapses. Curr Opin Neurobiol 17:387–393. doi:10.1016/j.conb.2007.04.012
19. Araque A, Carmignoto G, Haydon PG (2001) Dynamic signaling between astrocytes and neurons. Annu Rev Physiol 63:795–813. doi:10.1146/annurev.physiol.63.1.795
20. Chefer VI, Thompson AC, Zapata A, Shippenberg TS (2009) Overview of brain microdialysis. Curr Protoc Neurosci. Chapter 7:Unit7.1. doi: 10.1002/0471142301.ns0701s47
21. McLamore ES, Mohanty S, Shi J et al (2010) A self-referencing glutamate biosensor for measuring real time neuronal glutamate flux. J Neurosci Methods 189:14–22. doi:10.1016/j.jneumeth.2010.03.001
22. Namiki S, Sakamoto H, Iinuma S et al (2007) Optical glutamate sensor for spatiotemporal analysis of synaptic transmission. Eur J Neurosci 25:2249–2259. doi:10.1111/j.1460-9568.2007.05511.x
23. Brun MA, Tan K-T, Griss R et al (2012) A semisynthetic fluorescent sensor protein for glutamate. J Am Chem Soc 134:7676–7678. doi:10.1021/ja3002277
24. Takikawa K, Asanuma D, Namiki S et al (2014) High-throughput development of a hybrid-type fluorescent glutamate sensor for analysis of synaptic transmission. Angew Chem Int Ed 53:13439–13443. doi:10.1002/anie.201407181
25. Oldenziel WH, Beukema W, Westerink BHC (2004) Improving the reproducibility of hydrogel-coated glutamate microsensors by using an automated dipcoater. J Neurosci Methods 140:117–126. doi:10.1016/j.jneumeth.2004.04.038
26. Rahman MA, Kwon N-H, Won M-S et al (2005) Functionalized conducting polymer as an enzyme-immobilizing substrate: an amperometric glutamate microbiosensor for in vivo measurements. Anal Chem 77:4854–4860. doi:10.1021/ac050558v
27. Hu Y, Mitchell KM, Albahadily FN et al (1994) Direct measurement of glutamate release in the brain using a dual enzyme-based electrochemical sensor. Brain Res 659:117–125
28. Broussard GJ, Liang R, Tian L (2014) Monitoring activity in neural circuits with genetically encoded indicators. Front Mol Neurosci. doi:10.3389/fnmol.2014.00097

29. Lin MZ, Schnitzer MJ (2016) Genetically encoded indicators of neuronal activity. Nat Neurosci 19:1142–1153. doi:10.1038/nn.4359
30. Nakai J, Ohkura M, Imoto K (2001) A high signal-to-noise Ca2+ probe composed of a single green fluorescent protein. Nat Biotechnol 19:137–141. doi:10.1038/84397
31. Tallini YN, Ohkura M, Choi B-R et al (2006) Imaging cellular signals in the heart in vivo: cardiac expression of the high-signal Ca2+ indicator GCaMP2. Proc Natl Acad Sci U S A 103:4753–4758. doi:10.1073/pnas.0509378103
32. Tian L, Hires SA, Mao T et al (2009) Imaging neural activity in worms, flies and mice with improved GCaMP calcium indicators. Nat Methods 6:875–881. doi:10.1038/nmeth.1398
33. Akerboom J, Chen T-W, Wardill TJ et al (2012) Optimization of a GCaMP calcium indicator for neural activity imaging. J Neurosci 32:13819–13840. doi:10.1523/JNEUROSCI.2601-12.2012
34. Chen T-W, Wardill TJ, Sun Y et al (2013) Ultrasensitive fluorescent proteins for imaging neuronal activity. Nature 499:295–300. doi:10.1038/nature12354
35. Baird GS, Zacharias DA, Tsien RY (1999) Circular permutation and receptor insertion within green fluorescent proteins. Proc Natl Acad Sci U S A 96:11241–11246. doi:10.1073/pnas.96.20.11241
36. Wang Q, Shui B, Kotlikoff MI, Sondermann H (2008) Structural basis for calcium sensing by GCaMP2. Structure 16:1817–1827. doi:10.1016/j.str.2008.10.008
37. Petreanu L, Gutnisky DA, Huber D et al (2012) Activity in motor-sensory projections reveals distributed coding in somatosensation. Nature 489:299–303. doi:10.1038/nature11321
38. Shigetomi E, Bushong EA, Haustein MD et al (2013) Imaging calcium microdomains within entire astrocyte territories and endfeet with GCaMPs expressed using adeno-associated viruses. J Gen Physiol 141:633–647. doi:10.1085/jgp.201210949
39. Issa JB, Haeffele BD, Agarwal A et al (2014) Multiscale optical Ca2+ imaging of tonal organization in mouse auditory cortex. Neuron 83:944–959. doi:10.1016/j.neuron.2014.07.009
40. Vanni MP, Murphy TH (2014) Mesoscale transcranial spontaneous activity mapping in GCaMP3 transgenic mice reveals extensive reciprocal connections between areas of somatomotor cortex. J Neurosci 34:15931–15946. doi:10.1523/JNEUROSCI.1818-14.2014
41. Murakami T, Yoshida T, Matsui T, Ohki K (2015) Wide-field Ca2+ imaging reveals visually evoked activity in the retrosplenial area. Front Mol Neurosci. doi:10.3389/fnmol.2015.00020
42. Sun XR, Badura A, Pacheco DA et al (2013) Fast GCaMPs for improved tracking of neuronal activity. Nat Commun 4:2170. doi:10.1038/ncomms3170
43. Helassa N, Zhang X, Conte I et al (2015) Fast-response calmodulin-based fluorescent indicators reveal rapid intracellular calcium dynamics. Sci Rep 5:15978. doi:10.1038/srep15978
44. Huber D, Gutnisky DA, Peron S et al (2012) Multiple dynamic representations in the motor cortex during sensorimotor learning. Nature 484:473–478. doi:10.1038/nature11039
45. Ziv Y, Burns LD, Cocker ED et al (2013) Long-term dynamics of CA1 hippocampal place codes. Nat Neurosci 16:264–266. doi:10.1038/nn.3329
46. Vogt N (2015) Voltage sensors: challenging, but with potential. Nat Methods 12:921–924. doi:10.1038/nmeth.3591
47. Fioravante D, Regehr WG (2011) Short-term forms of presynaptic plasticity. Curr Opin Neurobiol 21:269–274. doi:10.1016/j.conb.2011.02.003
48. Xie Y, Chan AW, McGirr A et al (2016) Resolution of high-frequency mesoscale intracortical maps using the genetically encoded glutamate sensor iGluSnFR. J Neurosci 36:1261–1272. doi:10.1523/JNEUROSCI.2744-15.2016
49. Vyleta NP, Smith SM (2011) Spontaneous glutamate release is independent of calcium influx and tonically activated by the calcium-sensing receptor. J Neurosci 31:4593–4606. doi:10.1523/JNEUROSCI.6398-10.2011
50. Schellenberg GD, Furlong CE (1977) Resolution of the multiplicity of the glutamate and aspartate transport systems of Escherichia coli. J Biol Chem 252:9055–9064
51. Dwyer MA, Hellinga HW (2004) Periplasmic binding proteins: a versatile superfamily for protein engineering. Curr Opin Struct Biol 14:495–504. doi:10.1016/j.sbi.2004.07.004
52. Okumoto S, Looger LL, Micheva KD et al (2005) Detection of glutamate release from neurons by genetically encoded surface-displayed FRET nanosensors. Proc Natl Acad Sci U S A 102:8740–8745. doi:10.1073/pnas.0503274102
53. Hires SA, Zhu Y, Tsien RY (2008) Optical measurement of synaptic glutamate spillover and reuptake by linker optimized glutamate-sensitive fluorescent reporters. Proc Natl Acad Sci U S A 105:4411–4416. doi:10.1073/pnas.0712008105

54. Marvin JS, Borghuis BG, Tian L et al (2013) An optimized fluorescent probe for visualizing glutamate neurotransmission. Nat Methods 10:162–170. doi:10.1038/nmeth.2333
55. Marvin JS, Schreiter ER, Echevarría IM, Looger LL (2011) A genetically encoded, high-signal-to-noise maltose sensor. Proteins 79:3025–3036. doi:10.1002/prot.23118
56. Brunert D, Tsuno Y, Rothermel M et al (2016) Cell-type-specific modulation of sensory responses in olfactory bulb circuits by serotonergic projections from the raphe nuclei. J Neurosci 36:6820–6835. doi:10.1523/JNEUROSCI.3667-15.2016
57. Borghuis BG, Marvin JS, Looger LL, Demb JB (2013) Two-photon imaging of nonlinear glutamate release dynamics at bipolar cell synapses in the mouse retina. J Neurosci 33:10972–10985. doi:10.1523/JNEUROSCI.1241-13.2013
58. Borghuis BG, Looger LL, Tomita S, Demb JB (2014) Kainate receptors mediate signaling in both transient and sustained OFF bipolar cell pathways in mouse retina. J Neurosci 34:6128–6139. doi:10.1523/JNEUROSCI.4941-13.2014
59. Yonehara K, Farrow K, Ghanem A et al (2013) The first stage of cardinal direction selectivity is localized to the dendrites of retinal ganglion cells. Neuron 79:1078–1085. doi:10.1016/j.neuron.2013.08.005
60. Baxter PS, Bell KFS, Hasel P et al (2015) Synaptic NMDA receptor activity is coupled to the transcriptional control of the glutathione system. Nat Commun 6:6761. doi:10.1038/ncomms7761
61. O'Herron P, Chhatbar PY, Levy M et al (2016) Neural correlates of single-vessel haemodynamic responses in vivo. Nature. doi:10.1038/nature17965
62. Bao H, Goldschen-Ohm M, Jeggle P et al (2016) Exocytotic fusion pores are composed of both lipids and proteins. Nat Struct Mol Biol 23:67–73. doi:10.1038/nsmb.3141
63. Poleg-Polsky A, Diamond JS (2016) Retinal circuitry balances contrast tuning of excitation and inhibition to enable reliable computation of direction selectivity. J Neurosci 36:5861–5876. doi:10.1523/JNEUROSCI.4013-15.2016
64. Zhang R, Li X, Kawakami K, Du J (2016) Stereotyped initiation of retinal waves by bipolar cells via presynaptic NMDA autoreceptors. Nat Commun 7:12650. doi:10.1038/ncomms12650
65. Haustein MD, Kracun S, X-H L et al (2014) Conditions and constraints for astrocyte calcium signaling in the hippocampal mossy fiber pathway. Neuron 82:413–429. doi:10.1016/j.neuron.2014.02.041
66. Rosa JM, Bos R, Sack GS et al (2015) Neuron-glia signaling in developing retina mediated by neurotransmitter spillover. eLife 4:e09590. doi:10.7554/eLife.09590
67. Stork T, Sheehan A, Tasdemir-Yilmaz OE, Freeman MR (2014) Neuron-glia interactions through the heartless FGF receptor signaling pathway mediate morphogenesis of drosophila astrocytes. Neuron 83:388–403. doi:10.1016/j.neuron.2014.06.026
68. Parsons MP, Vanni MP, Woodard CL et al (2016) Real-time imaging of glutamate clearance reveals normal striatal uptake in Huntington disease mouse models. Nat Commun 7:11251. doi:10.1038/ncomms11251
69. Poskanzer KE, Yuste R (2016) Astrocytes regulate cortical state switching in vivo. Proc Natl Acad Sci U S A 113:E2675–E2684. doi:10.1073/pnas.1520759113
70. Looger LL, Griesbeck O (2012) Genetically encoded neural activity indicators. Curr Opin Neurobiol 22:18–23. doi:10.1016/j.conb.2011.10.024
71. Akerboom J, Tian L, Marvin J, Looger L (2012) Engineering and application of genetically encoded calcium indicators. In: Martin J-R (ed) Genetically encoded functional indicators. Humana Press, New York, pp 125–147
72. Moretti R, Bender BJ, Allison B, Meiler J (2016) Rosetta and the design of ligand binding sites. Methods Mol Biol 1414:47–62. doi:10.1007/978-1-4939-3569-7_4
73. Pettersen EF, Goddard TD, Huang CC et al (2004) UCSF Chimera—a visualization system for exploratory research and analysis. J Comput Chem 25:1605–1612. doi:10.1002/jcc.20084
74. Bender BJ, Cisneros A, Duran AM et al (2016) Protocols for molecular modeling with Rosetta3 and RosettaScripts. Biochemistry 55:4748–4763. doi:10.1021/acs.biochem.6b00444
75. Hughes MD, Nagel DA, Santos AF et al (2003) Removing the redundancy from randomised gene libraries. J Mol Biol 331:973–979
76. Edelheit O, Hanukoglu A, Hanukoglu I (2009) Simple and efficient site-directed mutagenesis using two single-primer reactions in parallel to generate mutants for protein structure-function studies. BMC Biotechnol 9:61. doi:10.1186/1472-6750-9-61
77. Liu H, Naismith JH (2008) An efficient one-step site-directed deletion, insertion, single and multiple-site plasmid mutagenesis protocol. BMC Biotechnol 8:91. doi:10.1186/1472-6750-8-91
78. Quan J, Tian J (2011) Circular polymerase extension cloning for high-throughput cloning

of complex and combinatorial DNA libraries. Nat Protoc 6:242–251. doi:10.1038/nprot.2010.181

79. Kunkel TA (1985) Rapid and efficient site-specific mutagenesis without phenotypic selection. Proc Natl Acad Sci U S A 82:488–492
80. Huang R, Fang P, Kay BK (2012) Improvements to the Kunkel mutagenesis protocol for constructing primary and secondary phage-display libraries. Methods 58:10–17. doi:10.1016/j.ymeth.2012.08.008
81. Cadwell RC, Joyce GF (1992) Randomization of genes by PCR mutagenesis. Genome Res 2:28–33. doi:10.1101/gr.2.1.28
82. Gruet A, Longhi S, Bignon C (2012) One-step generation of error-prone PCR libraries using Gateway® technology. Microb Cell Factories 11:14. doi:10.1186/1475-2859-11-14
83. Drobizhev M, Makarov NS, Tillo SE et al (2011) Two-photon absorption properties of fluorescent proteins. Nat Methods 8:393–399. doi:10.1038/nmeth.1596
84. Makarov NS, Drobizhev M, Rebane A (2008) Two-photon absorption standards in the 550–1600 nm excitation wavelength range. Opt Express 16:4029–4047. doi:10.1364/OE.16.004029
85. Vandenberghe LH, Xiao R, Lock M et al (2010) Efficient serotype-dependent release of functional vector into the culture medium during adeno-associated virus manufacturing. Hum Gene Ther 21:1251–1257. doi:10.1089/hum.2010.107
86. Paxinos G, Franklin KBJ (2012) Paxinos and Franklin's the mouse brain in stereotaxic coordinates, 4th edn. Academic Press, Amsterdam
87. Deverman BE, Pravdo PL, Simpson BP et al (2016) Cre-dependent selection yields AAV variants for widespread gene transfer to the adult brain. Nat Biotechnol 34:204–209. doi:10.1038/nbt.3440
88. Chia TH, Levene MJ (2009) Microprisms for in vivo multilayer cortical imaging. J Neurophysiol 102:1310–1314. doi:10.1152/jn.91208.2008
89. Low RJ, Gu Y, Tank DW (2014) Cellular resolution optical access to brain regions in fissures: imaging medial prefrontal cortex and grid cells in entorhinal cortex. Proc Natl Acad Sci U S A 111:18739–18744. doi:10.1073/pnas.1421753111
90. Guo ZV, Hires SA, Li N, O'Connor DH, Komiyama T, Ophir E, Huber D, Bonardi C, Morandell K, Gutnisky D, Peron S, Xu N-l, Cox J, Svoboda K (2014) Procedures for behavioral experiments in head-fixed mice. PLoS One 9(2). doi:10.1371/journal.pone.0088678
91. Kislin M, Mugantseva E, Molotkov D, Kulesskaya N, Khirug S, Kirilkin I, Pryazhnikov E, Kolikova J, Toptunov D, Yuryev M, Giniatullin R, Voikar V, Rivera C, Rauvala H, Khiroug L (2014) Flat-floored air-lifted platform: a new method for combining behavior with microscopy or electrophysiology on awake freely moving rodents. J Vis Exp 88:–e51869. doi:10.3791/51869
92. Urbain N, Gervasoni D, Soulière F et al (2000) Unrelated course of subthalamic nucleus and globus pallidus neuronal activities across vigilance states in the rat. Eur J Neurosci 12:3361–3374
93. Urbain N, Salin PA, Libourel P-A et al (2015) Whisking-related changes in neuronal firing and membrane potential dynamics in the somatosensory thalamus of awake mice. Cell Rep 13:647–656. doi:10.1016/j.celrep.2015.09.029
94. Guizar-Sicairos M, Thurman ST, Fienup JR (2008) Efficient subpixel image registration algorithms. Opt Lett 33(2):156–158
95. Wu M, Chen R, Soh J, Shen Y, Jiao L, Wu J, Chen X, Ji R, Hong M (2016) Super-focusing of center-covered engineered microsphere. Sci Rep 6:31637. doi:10.1038/srep31637
96. Granseth B, Odermatt B, Royle SJ, Lagnado L (2006) Clathrin-mediated endocytosis is the dominant mechanism of vesicle retrieval at hippocampal synapses. Neuron 51:773–786. doi:10.1016/j.neuron.2006.08.029
97. Shen Y, Lai T, Campbell RE (2015) Red fluorescent proteins (RFPs) and RFP-based biosensors for neuronal imaging applications. Neurophotonics 2:031203. doi:10.1117/1.NPh.2.3.031203
98. Dana H, Mohar B, Sun Y et al (2016) Sensitive red protein calcium indicators for imaging neural activity. Elife. doi:10.7554/eLife.12727
99. Lin JY, Knutsen PM, Muller A et al (2013) ReaChR: a red-shifted variant of channelrhodopsin enables deep transcranial optogenetic excitation. Nat Neurosci 16:1499–1508. doi:10.1038/nn.3502
100. Drobizhev M, Tillo S, Makarov NS, Hughes TE, Rebane A (2009) Absolute two-photon absorption spectra and two-photon brightness of orange and red fluorescent proteins. J Phys Chem B 113(4):855–859. doi:10.1021/jp8087379